AGU PUBLICATIONS

JGR

Journal of Geophysical Research: Solid Earth

RESEARCH ARTICLE
10.1002/2015JB012322

Key Points:
- Nucleation occurs at stress heterogeneities; thermal pressurization then sustains dynamic rupture
- Thermal pressurization can sustain rupture on faults with low shear stress
- Slight differences in shear stress result in different rupture modes

Correspondence to:
S. V. Schmitt,
stuart@stuartschmitt.com

Citation:
Schmitt, S. V., P. Segall, and E. M. Dunham (2015), Nucleation and dynamic rupture on weakly stressed faults sustained by thermal pressurization, *J. Geophys. Res. Solid Earth*, *120*, doi:10.1002/2015JB012322.

Received 30 JUN 2015
Accepted 22 SEP 2015
Accepted article online 6 OCT 2015

Nucleation and dynamic rupture on weakly stressed faults sustained by thermal pressurization

Stuart V. Schmitt[1,2], Paul Segall[1], and Eric M. Dunham[1,3]

[1]Department of Geophysics, Stanford University, Stanford, California, USA, [2]Now at Chevron Energy Technology Company, Houston, Texas, USA, [3]Institute for Computational and Mathematical Engineering, Stanford University, Stanford, California, USA

Abstract Earthquake nucleation requires that the shear stress τ locally reaches a fault's static strength, $f\sigma_{\text{eff}}$, the product of the friction coefficient and effective normal stress. Once rupture initiates, shear heating-induced thermal pressurization can sustain rupture at much lower τ/σ_{eff} ratios, a stress condition believed to be the case during most earthquakes. This requires that earthquakes nucleate at heterogeneities. We model nucleation and dynamic rupture on faults in a 2-D elastic medium with rate/state friction and thermal pressurization, subjected to globally low τ but with local stress heterogeneities that permit nucleation. We examine end-member cases of either high-τ or low-σ_{eff} heterogeneities. We find that thermal pressurization can sustain slip at τ/σ_{eff} values as low as 0.13, compared to static friction of ~0.7. Background τ (and, to lesser extent, heterogeneity width) controls whether ruptures arrest or are sustained, with extremely low values resulting in arrest. For a small range of background τ, sustained slip is pulse-like. Cessation of slip in a pulse tail can result from either diffusive restrengthening of σ_{eff} or a wave-mediated stopping phase that follows the rupture tip. Slightly larger background τ leads to sustained crack-like rupture. Thermal pressurization is stronger at high-τ heterogeneities, resulting in a lower background τ threshold for sustained rupture and potentially larger arresting ruptures. High-stress events also initiate with higher moment rate, although this may be difficult to observe in nature. For arresting ruptures, stress drops and the dependence of fracture energy on mean slip are both consistent with values inferred for small earthquakes.

1. Introduction

Laboratory rock sliding experiments [*Byerlee*, 1978] show that for most rock types, the friction coefficient ($f = \tau/\sigma_{\text{eff}}$) at which slip initiates is about 0.6–0.8. At lithostatic normal stress and hydrostatic pore pressure, Byerlee's observation suggests that the shear strength of faults exceeds ~100 MPa at seismogenic depths on continental strike-slip faults. However, *Brune et al.* [1969] showed that frictional sliding at $\tau \gtrsim 10$ MPa would produce a heat flow anomaly that is not observed in field data adjacent to the San Andreas fault [*Lachenbruch and Sass*, 1980]. Temperature measurements in boreholes drilled across faults shortly after earthquakes also indicate low shear traction during seismic slip [*Kano et al.*, 2006; *Fulton et al.*, 2010, 2013].

To explain earthquake slip at low τ, *Sibson* [1973] proposed that shear heating-induced thermal pressurization of pore fluid leads to a strong dynamic reduction in τ. First proposed for landslides [*Habib*, 1967], frictional heating increases pore fluid pressure and causes $\sigma_{\text{eff}} = \sigma - p$ to decrease, provided that pore pressure diffusion or fault zone dilatancy does not balance pressurization. *Lachenbruch* [1980] predicted that thermal pressurization could lead to a significant loss of shear strength under certain circumstances. *Mase and Smith* [1985, 1987] coupled the transport equations with an imposed slip history and found that thermal pressurization is indeed likely to strongly reduce τ during seismic slip. Many further studies have also investigated this process [*Lee and Delaney*, 1987; *Andrews*, 2002; *Bizzarri and Cocco*, 2006a, 2006b; *Suzuki and Yamashita*, 2006; *Rice*, 2006].

Dynamic weakening can permit slip on faults stressed below their static strength [e.g., *Melosh*, 1979]. Measurements of crustal stresses support this scenario; on the San Andreas fault, borehole breakouts, earthquake focal mechanisms, and hydrofrac orientations show that the regional maximum horizontal stress is at a high angle to the fault strike [*Zoback et al.*, 1987]. *Townend and Zoback* [2004] reported maximum stress orientations from 68°±7° in Southern California to 85° in Northern California, which implies a τ/σ_{eff} ratio

ranging from 0.1 to 0.4. From focal mechanisms, similar observations have been made in the Marlborough fault system in New Zealand [*Balfour et al.*, 2005], near the Denali Fault in Alaska [*Ratchkovski*, 2003], and near the North Anatolian Fault in Turkey [*Heidbach et al.*, 2008].

The observation that earthquakes often take the form of slip pulses is consistent with dynamic weakening during seismic slip on faults with low shear stress. *Heaton* [1990] noted that large earthquakes have slip rise times much shorter than the event durations and concluded that earthquakes take the form of slip pulses, similar to models proposed by *Broberg* [1978] and *Freund* [1979]. *Cochard and Madariaga* [1994], *Perrin et al.* [1995], and *Zheng and Rice* [1998] found slip pulses in numerical simulations with fault constitutive relationships that include strong velocity weakening and weakly prestressed faults. It should be noted, however, that short slip rise times can result from arrest waves from fault edges [*Day*, 1982; *Johnson*, 1990], heterogeneous fault properties [*Beroza and Mikumo*, 1996], material contrasts across the fault [*Andrews and Ben-Zion*, 1997], and low-velocity fault zones [*Huang and Ampuero*, 2011]. *Perrin et al.* [1995] found that a constitutive law that allows rapid restrengthening is required for steady state pulses to exist. *Garagash* [2012] demonstrated that thermal pressurization is capable of sustaining steady pulses due to diffusive restrengthening.

Laboratory studies at low slip speeds (0.1–100 μm/s) yielded friction laws (starting with *Dieterich* [1979] and *Ruina* [1983]) in which f depends on slip rate and slip. Rate- and state-dependent friction laws have provided plausible mechanisms for earthquake nucleation, steady creep, and postseismic slip [*Dieterich*, 1992, 1994; *Marone*, 1998]. Some efforts have been made to incorporate rate/state friction into models of dynamic slip [e.g., *Okubo*, 1989; *Lapusta et al.*, 2000]; however, the evidence for rapid slip at low τ argues for an additional weakening mechanism. *Perrin et al.* [1995] and *Zheng and Rice* [1998] adopted a friction law in which steady state friction undergoes strong dynamic weakening, but they did not model the quasi-static nucleation phase. *Bizzarri and Cocco* [2006a, 2006b] and *Noda et al.* [2009] similarly modeled dynamic rupture with rate- and state-dependent friction following imposed nucleation, both including thermal pressurization and the latter including strong dynamic weakening. *Noda and Lapusta* [2010] modeled both nucleation and dynamic rupture in cycle models with rate/state friction and thermal pressurization on 3-D faults with spatially variable transport and frictional properties.

To reconcile the high static strength of faults with low overall stress levels and low dynamic strength, the most likely scenario is that earthquakes nucleate at local stress or strength heterogeneities and then, sustained by dynamic weakening, propagate into regions of low τ. *Noda and Lapusta*'s [2010] simulations are consistent with this, in that nucleation always occurs at sites with high shear stress. Those sites coincided with locations where prior earthquake stress drops were small due to less-effective thermal pressurization during dynamic rupture. Across a wide range of mechanical and hydrothermal properties, however, *Schmitt et al.* [2011] found in 2-D numerical simulations with rate/state frictional nucleation that thermal pressurization can become a significant weakening mechanism late in the quasi-static nucleation phase. That study imposed spatially uniform stresses, which results in unrealistically large stress drops due to thermal pressurization decreasing shear strength to near zero. In this work we combine modeling of rate- and state-dependent nucleation with dynamic rupture, incorporating thermal pressurization during all phases. We develop physically motivated simulations in which slip nucleates spontaneously in response to accumulating stress. Defining $\bar{\sigma}$ to be the nominal value of σ_{eff} in the absence of thermal pressurization, we investigate idealized models in which a nucleation zone with high $\tau/\bar{\sigma}$ is embedded in a fault with low $\tau/\bar{\sigma}$.

We start by presenting the conceptual model of faults and the mathematical description of the coupled thermomechanical system. We then present a brief description of the nucleation phase followed by a description of the transition to dynamic rupture, during which thermal pressurization becomes dominant. We then present sample numerical simulations. Following the examples, we present observations derived from our entire suite of simulations, with implications for models of source parameters and energy budgets of earthquakes.

2. Model Description

Our model consists of a fault subjected to antiplane shear embedded in a fluid-saturated porous medium, shown schematically in Figure 1. We assume uniform diffusive properties, but the model is motivated by observations of fault zones in Japan and Southern California with more complex structure. *Wibberley and Shimamoto* [2003] measured permeability across Japan's Median Tectonic Line and found a low-permeability ($\sim 10^{-19}$ m^2 at 80–180 MPa confining pressure) fault core of width ~0.1 m surrounded by

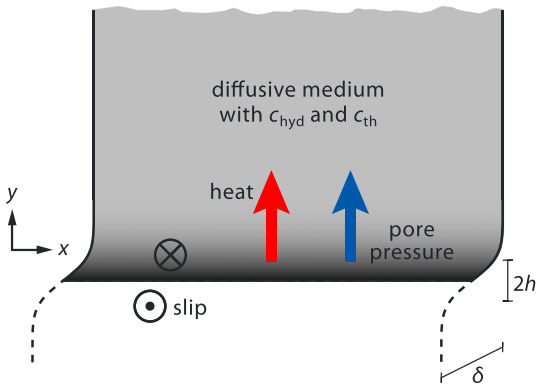

Figure 1. Schematic of our model. Fault slip is antiplane and distributed over a shear zone with a Gaussian strain distribution. Because of symmetry, only one side is modeled.

a higher-permeability (10^{-16} to 10^{-14} m^2) damage zone. *Lockner et al.* [2000] found similar values for core samples from 1500 m depth on the Nojima fault. The observed permeabilities yield a hydraulic diffusivity $c_{hyd} \approx 10^{-6}$ m^2/s. Diffusivity of that magnitude yields a characteristic diffusion length $\sqrt{4c_{hyd}t}$ of ~0.01 m for tens of seconds of slip, which suggests that the pore pressure boundary layer that results from shear heating is much smaller than the width of the fault core. We therefore neglect the distant higher-permeability region in our simulations. In the following sections, we describe the governing equations of our model. Material properties and initial conditions are summarized in Table 1.

2.1. Heat and Pore Fluid Transport

The fluid-saturated porous medium flanking the fault transports both heat and pore pressure. The governing equations for their source and transport are derived in detail in *Rice* [2006] and *Segall and Rice* [2006]. For spatially uniform properties, the equation for thermal diffusion with a distributed shear heating source is

$$\tau \frac{\partial \gamma}{\partial t} + k_{th} \frac{\partial^2 T}{\partial y^2} = \rho c_v \frac{\partial T}{\partial t}, \quad (1)$$

where T is temperature, γ is shear strain, ρ is the bulk density, k_{th} is thermal conductivity, and c_v is the heat capacity. We use $\rho c_v = 2.7$ MPa/K and $k_{th} = 1.89$ MPa mm^2/(Ks) to be consistent with the values chosen by *Noda et al.* [2009]. We neglect advection of heat, which is supported by *Vredevoogd et al.* [2007]. Shear heating

Table 1. Parameters Used in This Work

Parameters	Symbols	Values
Elastic properties		
Shear modulus	μ	30 GPa
Shear wave speed	c_s	3000 m/s
Density	ρ	3333.33 kg/m^3
Shear zone width	h	50 μm
Friction properties		
Reference velocity	v_0	1 μm/s
Steady state friction at v_0	f_0	0.7
Direct velocity strengthening magnitude	a	0.016
State effect magnitude	b	0.020
State evolution distance	d_c	20 μm
Hydrothermal properties		
Specific heat capacity	c_v	810 J/kgK
Thermal conductivity	k_{th}	1.89 MPa mm^2/K/s
Thermal diffusivity	c_{th}	0.7 mm^2/s
Hydraulic diffusivity	c_{hyd}	2.988 mm^2/s
Thermal pressurization coefficient	Λ	0.468 MPa/K
Stress conditions		
Normal stress	σ	196 MPa
Nominal pore pressure	p_0	70 MPa
Background shear stress	τ_{bg}	0.97–21.42 MPa

occurs over a finite zone with a Gaussian distribution of strain with half-width h, so it is related to slip velocity v through the relationship [*Rice*, 2006]

$$\frac{\partial\gamma(y,t)}{\partial t} = \frac{v(t)}{h\sqrt{2\pi}} \exp\left(-\frac{y^2}{2h^2}\right) . \tag{2}$$

We use $h = 50$ μm, which is again consistent with *Noda et al.* [2009]. During an earthquake, the transient rises in pore pressure and temperature have a small spatial extent compared to the along-fault length scale, which allows us to neglect diffusion in the latter dimension.

Pore pressure transport is treated as a diffusion process; dilatancy [*Segall and Rice*, 1995] is neglected. Pore pressure satisfies

$$\frac{\partial p}{\partial t} = c_{\text{hyd}} \frac{\partial^2 p}{\partial y^2} + \Lambda \frac{\partial T}{\partial t} , \tag{3}$$

again neglecting diffusion in the x dimension. The hydraulic diffusivity c_{hyd} is related to permeability k_{hyd} via

$$c_{\text{hyd}} = \frac{k_{\text{hyd}}}{\phi(\beta_f + \beta_\phi)\eta} , \tag{4}$$

where ϕ is porosity, β_f is the pore fluid compressibility, β_ϕ is the pore compressibility (which depends on pore shape), and η is the pore fluid viscosity. The source term in equation (3) is thermal pressurization, and the coefficient is defined as

$$\Lambda = \frac{\lambda_f - \lambda_\phi}{\beta_f + \beta_\phi} \tag{5}$$

[*Rice*, 2006], where λ_f and λ_ϕ are thermal expansivities of the pore fluid and pores, respectively. To be consistent with *Noda et al.* [2009], we use Λ =0.468 MPa/K.

2.2. Elasticity and Fault Friction

For a planar fault in a homogeneous 2-D medium, the equation of motion is

$$\tau(x,t) = \tau_0(x,t) - \frac{\mu}{2c_s} v(x,t) + \psi(x,t) . \tag{6}$$

In equation (6), $\tau_0(x,t)$ is the shear stress in the absence of slip or, in other words, the prestress and remote loading stress. The remaining terms denote elastic interactions; $\mu v(x,t)/2c_s$ is "radiation damping," while $\psi(x,t)$ is the elastodynamic stress transfer function [*Rice*, 1993; *Perrin et al.*, 1995; *Geubelle and Rice*, 1995], which integrates to zero across the entire fault. Radiation damping is the stress change resulting from radiation of plane S waves away from the fault. Therefore, the interpretation of equation (6) is that the shear stress on the fault is equal to the initial load minus a stress change resulting from sliding, plus the transfer of stress due to spatially variable slip. At low slip speeds (which correspond to slow evolution of slip zone size), the stress interaction is effectively instantaneous and may be approximated as a Hilbert transform of the slip gradient [*Segall*, 2010, chap. 4], which we use to simplify computation of the quasi-static nucleation phase.

The frictional resistance to sliding is given by

$$\tau = f(v,\theta)\sigma_{\text{eff}} , \tag{7}$$

where the friction coefficient depends on slip rate v and state θ, which has dimension of time. We use the regularized rate- and state-dependent form of the friction law [*Rice et al.*, 2001],

$$f(v,\theta) = a \operatorname{arsinh}\left[\frac{v}{2v_0} \exp\left(\frac{f_0}{a} + \frac{b}{a} \ln\frac{v_0\theta}{d_c}\right)\right] . \tag{8}$$

The parameter f_0 is the steady state ($\dot{\theta} = 0$) friction at reference velocity v_0, and d_c is the characteristic slip distance for evolution of θ. Equation (8) is well behaved as $v \to 0$ and allows for nonpositive values of v, which occurs in a few of our simulations. When the argument of the arsinh is large compared to unity (or alternatively, when $f \gg a$), equation (8) reduces to

$$f(v,\theta) = f_0 + a \ln\frac{v}{v_0} + b \ln\frac{v_0\theta}{d_c} \tag{9}$$

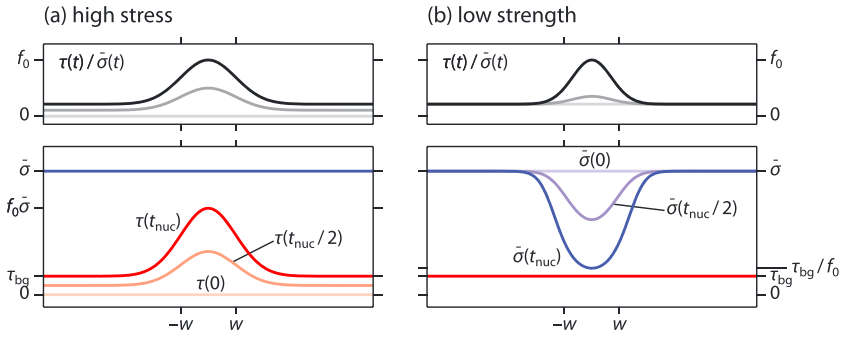

Figure 2. Models of τ/σ_{eff} heterogeneity. In both Figures 2a and 2b, the upper plot is $\tau_0(x,t)/\bar{\sigma}(x,t)$ at times $t = 0$, t', and $2t'$, while the lower plot shows τ_0 (red) and $\bar{\sigma}$ (blue) at those times. (a) High-stress model, in which τ_0 increases faster within a Gaussian-shaped region with half-width w. (b) Low-strength model, in which τ_0 is uniform and constant, while $\bar{\sigma}$ decreases in a manner that yields a Gaussian-shaped distribution of $\tau_0/\bar{\sigma}(x,t)$.

[*Ruina*, 1983]. At low-v, low-f conditions, equation (8) becomes

$$f(v,\theta) = \frac{av}{2v_0}\exp\left(\frac{f_0}{a} + \frac{b}{a}\ln\frac{v_0\theta}{d_c}\right), \tag{10}$$

which has dependence on both v and θ but is rate strengthening for all θ. In this study, we use $v_0 = 1$ μm/s and $f_0 = 0.7$, which yields a low-v fault strength consistent with *Byerlee's* [1978] observations. State evolution is described by the slip law [*Ruina*, 1983],

$$\frac{d\theta}{dt} = -\frac{|v|\theta}{d_c}\ln\frac{|v|\theta}{d_c}. \tag{11}$$

We neglect the other common state evolution law, the aging law ($\dot{\theta} = 1 - v\theta/d_c$), since the slip law is more consistent with frictional behavior at slip speeds occurring during nucleation [*Nakatani*, 2001; *Ampuero and Rubin*, 2008]. During steady state slip ($\dot{\theta} = 0$), equation (9) simplifies to

$$f(v) = f_0 + (a-b)\ln\frac{v}{v_0}, \tag{12}$$

which describes frictional behavior in the interior of nucleation zones and dynamic ruptures.

2.3. Stress Distribution, Loading, and Initial Conditions

Because our model accounts for high static strength of faults, nucleation of slip requires that $\tau \approx f_0\bar{\sigma}$ at the nucleation site, where $\bar{\sigma}$ is the initial effective normal stress. For the remainder of this paper, we distinguish between $\bar{\sigma}$ and the local effective normal stress $\sigma_{eff} = \bar{\sigma} - \Delta p$, which includes the transient pore pressure change. We consider two end-member models where $\tau/\bar{\sigma}$ locally favors nucleation (Figure 2). The first is a "high-stress" model in which $\bar{\sigma}$ is uniformly high, so fault strength $\sim f_0\bar{\sigma}$ is also uniformly high. The fault is loaded by a Gaussian-shaped region of elevated shear stress τ, and slip nucleation occurs when and where $\tau_0(x,t) \approx f_0\bar{\sigma}$. Away from the nucleation zone, however, τ remains low. The alternative end-member model is a "low-strength" model in which $\bar{\sigma}(x,t)$ locally declines—perhaps due to an increase in pore pressure—while τ is uniformly low.

Spatially varying tractions on faults with otherwise uniform material properties may arise from a number of processes. Stress heterogeneities in both σ and τ arise from nonplanar fault geometry [e.g., *Chester and Chester*, 2000]. On planar faults, prior slip events result in elevated τ at their tips. Locally elevated pore pressure results in a low-strength condition; this effect is often associated with fluid injection for disposal or reservoir stimulation. Natural origins of elevated pore pressure on faults, such as mineral dehydration [*Ague et al.*, 1998], have also been proposed. In contrast to natural and anthropogenic loading mechanisms, the two types of stress distribution in our models are highly idealized and are not intended to represent specific loading processes on real faults.

For slip to nucleate spontaneously, the fault loading must change gradually with time. We start with uniform initial conditions and gradually increase the amplitude of heterogeneities in τ_0 or $\bar{\sigma}$. In both models, the fault

is loaded such that the ratio $\tau_0(x)/\bar{\sigma}(x)$ has a Gaussian shape with half-width w. For the high-stress model, $\tau_0(x, t = 0) = 0$ and the loading $\dot{\tau}_0(x)$ has a Gaussian shape along-fault strike,

$$\tau_0(x, t) = \left[A + B \exp\left(-\frac{x^2}{2w^2}\right)\right] t \,. \tag{13}$$

In this paper, all high-stress simulations use $(A + B) = 0.02$ Pa/s in order to yield nucleation times of roughly a century and B is varied to yield different values of background stress $\tau_{bg} = \tau_0(x \gg w)$. In the low-strength model, $\tau_0 = \tau_{bg}$ for all (x, t), but $\bar{\sigma}$ changes such that

$$\bar{\sigma}(x, t) = \left[\frac{1}{\bar{\sigma}_{bg}} + \left(\frac{1}{\bar{\sigma}_{bg} - Ct} - \frac{1}{\bar{\sigma}_{bg}}\right) \exp\left(-\frac{x^2}{2w^2}\right)\right]^{-1} . \tag{14}$$

At $x = 0$, equation (14) simplifies to $\bar{\sigma}(0, t) = \bar{\sigma}_{bg} - Ct$. Thus, the minimum value of $\bar{\sigma}(x, t)$ decreases linearly in time. All low-strength simulations in this work employ $C = 0.03$ Pa/s.

For both nucleation methods, the initial conditions for friction are based on uniformly distributed slip speed of 10^{-15} m/s. Slip law nucleation takes the form of accelerating slip pulses (see section 4 below), and given perfectly symmetric initial conditions, the slip pulses accelerate bilaterally. *Ampuero and Rubin* [2008], however, showed that minute variations in initial conditions result in acceleration of only one pulse, which is likely a more realistic scenario. We therefore introduce a white noise component such that $v_{init}(x) = 10^{-15} \exp[\omega(x)]$ m/s, where $\omega(x)$ is normally distributed noise with standard deviation 0.003. Given the initial conditions in τ, $\bar{\sigma}$, and v, frictional state θ is thus set to be consistent with equations (7) and (8).

3. Nucleation Phase

3.1. Minimum Nucleation Zone Size

In rate- and state-dependent friction, a nucleation zone must be larger than a minimum length in order for slip to accelerate. A linear stability analysis [*Ruina*, 1983] about steady state shows that small perturbations in v become unstable if the nucleation zone's stiffness is less than the critical value

$$k_{crit} = \frac{(b - a)\bar{\sigma}}{d_c} \,. \tag{15}$$

Since the nucleation zone must evolve from below steady state ($v\theta/d_c < 1$) to above steady state, k_{crit} is a relevant upper bound for its stiffness. In an elastic continuum, $k \approx \mu/2L$, where L is the half-length of the slip zone. Thus, a minimum nucleation zone dimension can be defined [*Rubin and Ampuero*, 2005],

$$L_{min} = \frac{\mu d_c}{2(b - a)\bar{\sigma}} \,, \tag{16}$$

which is similar to h^* defined in *Rice* [1993] within a factor of $\pi/4$. It should be noted that different expressions for minimum nucleation zone size may correspond to cases with different a/b ratios or initial conditions in v and θ [*Ampuero and Rubin*, 2008]. For the heterogeneous stress distributions considered here, slip nucleation requires a region where $\tau \approx f_0\bar{\sigma}$ over a length greater than $2L_{min}$. More specifically, a region wider than $2L_{min}$ must reach steady state in order for slip to accelerate to seismic slip speeds.

In our loading scheme, the peak of the Gaussian distribution of $\tau/\bar{\sigma}$ at $x = 0$ is the first location where the fault becomes critically stressed (that is, $\tau_0 \approx f_0\bar{\sigma}$). The width of the critically stressed region then grows. The response of slip zones smaller than L_{min} is to slip stably. If slip magnitude is sufficient to allow significant state evolution, stress inside the nucleation zone will decrease quasi-statically, releasing some of the strain energy that loading imparted to the system. Figure 3 shows a nucleation simulation with $w = 2.5L_{min}$ where this stress reduction occurs. The values of v and a dimensionless measure of state S are shown for $x = 0$. The latter is defined as

$$S = \frac{1}{1 + \frac{d_c}{v\theta}} \,. \tag{17}$$

If $S > 0.5$, slip is above steady state, or in other words, slip is occurring but it has not yet been sufficient for θ to evolve to its steady state value. If $S = 0.5$, slip is at steady state, and $S \approx 0$ means the fault is far below steady state (usually by not slipping). In Figure 3, two episodes of slow slip occur, and the nucleation zone remains

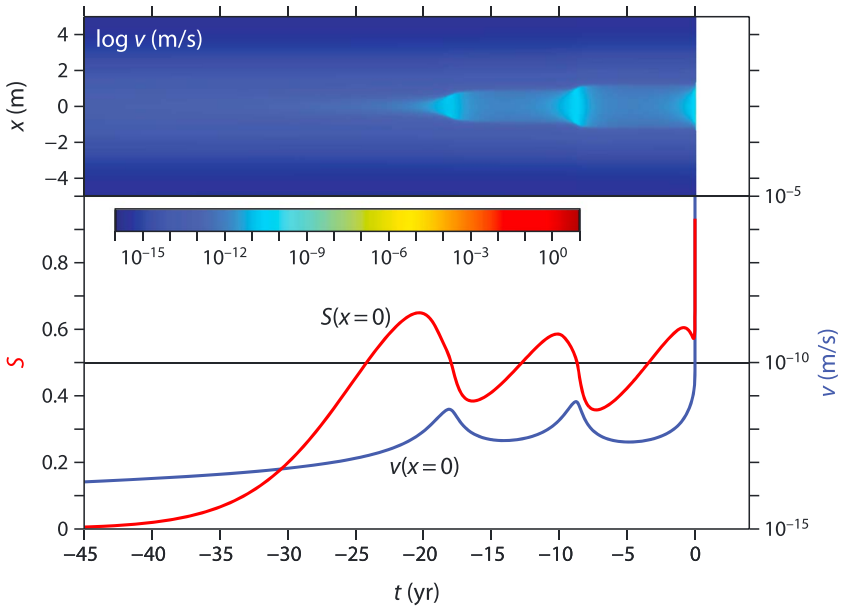

Figure 3. Example of nucleation with a stress heterogeneity that is insufficient for slip to accelerate monotonically to instability. Here $w = 2.5L_{\text{min}}$ and the high-stress loading conditions are applied. The upper space-time plot of log v shows the occurrence of slow slip events, and the lower plot shows $v(t)$ in blue and $S = 1/(1 + d_c/v\theta)$ in red, both located at $x = 0$. The nucleation zone oscillates about steady state (red curve near 0.5) for ~25 years, while loading increases the size of the critically loaded area. Eventually (at $t = 0$ year), the critically loaded area is sufficiently large to host unstable slip.

near steady state for several years until loading widens the critically stressed portion of the fault. While slip episodes like those in Figure 3 are of interest in other contexts (for example, *Liu and Rice* [2005] suggest that they might explain observed slow slip events), we avoid them by using sufficiently large w in order to maintain simple stress distributions at the onset of seismic slip.

In high-stress nucleation, we find that $w \gtrsim 3L_{\text{min}}$ is required for slip to accelerate directly to seismic speeds, without preceding slow slip events. In low-strength nucleation, $\bar{\sigma}$ varies spatially and with time, so it less obvious how to define L_{min}. Nucleation occurs at the location of minimum $\bar{\sigma}$ and when $\tau \approx f_0\bar{\sigma}_{\text{min}}$, so the minimum nucleation zone size is approximately

$$L_{\text{min}}^{\text{LS}} = \frac{\mu d_c f_0}{2(b-a)\tau} . \tag{18}$$

We find that $w \gtrsim 4L_{\text{min}}^{\text{LS}}$ is required for a low-strength nucleation zone to accelerate monotonically to seismic slip speeds. It is worth noting from equation (18) that lower shear stress levels require larger nucleation zones for low-strength nucleation, whereas L_{min} is independent of background shear stress for high-stress nucleation. The inverse scaling with τ has been found in other studies considering nucleation of rupture in response to decreases in $\bar{\sigma}$ [e.g., *Viesca and Rice*, 2012; *Garagash and Germanovich*, 2012]. As with high-stress nucleation, fast slip can occur in simulations where $w < 4L_{\text{min}}^{\text{LS}}$, but only after a protracted period of stable sliding at the center of the nucleation zone while the loading process grows the slip zone.

3.2. Thermal Pressurization During Nucleation

Earthquake nucleation in rate- and state-dependent friction is normally characterized as a process in which a region of a fault accelerates and weakens as a consequence of velocity-weakening behavior at steady state. By decreasing effective normal stress, thermal pressurization contributes additional weakening. *Schmitt et al.* [2011] identified conditions under which it is possible for thermal pressurization to dominate fault weakening at quasi-static ($v \lesssim 0.1$ m/s) slip speeds. To quantify the relative contributions of rate- and state-dependent friction and thermal pressurization to total fault weakening, *Schmitt et al.* [2011] examined the rate of change of shear strength

$$\frac{d\tau}{dt} = \frac{df}{dt}\sigma_{\text{eff}} - f\frac{dp}{dt} \approx \frac{df}{dt}\bar{\sigma} - f_0\frac{dp}{dt} . \tag{19}$$

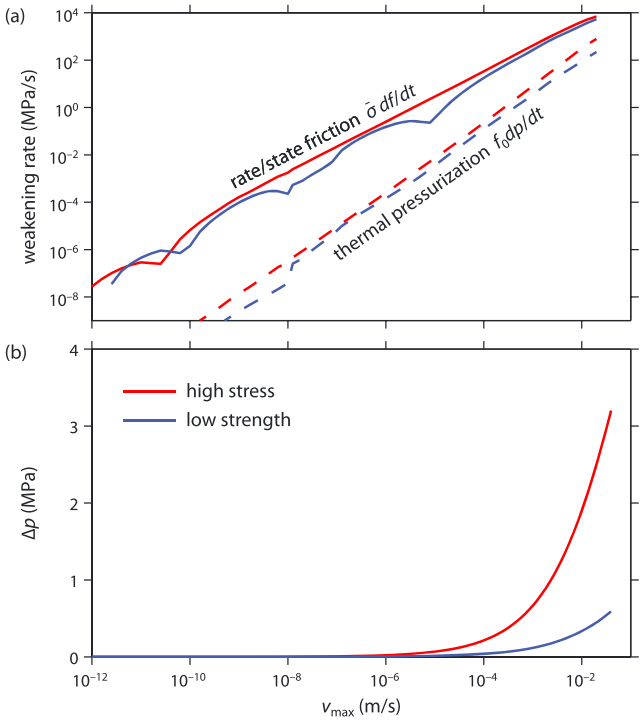

Figure 4. (a) Significant terms of equation (19) during quasi-static nucleation phase of both high-stress (red) and low-strength (blue) simulations, at the x coordinates corresponding to maximum magnitude of $\dot{\tau}$. Thermal pressurization (dashed lines) contributes less to $\dot{\tau}$ than rate- and state-dependent friction (solid lines). (b) Pore pressure on the fault resulting from thermal pressurization as slip accelerates during the nucleation phase.

During most of the nucleation phase, $|\dot{f}\bar{\sigma}| > |f_0\dot{p}|$, so rate- and state-dependent friction dominates fault weakening. *Segall and Rice* [2006] define a critical velocity v_{crit} when $\dot{p}$ grows to a condition where $|\dot{f}\bar{\sigma}| = |f_0\dot{p}|$, and then for $v > v_{crit}$, thermal pressurization dominates $\dot{\tau}$. Factors that enhance thermal pressurization during quasi-static slip include the following: aging law state evolution instead of slip law, large slip-weakening distance d_c, high static friction f_0, small shear zone thickness h, and low composite diffusivity $\left(\sqrt{c_{th}} + \sqrt{c_{hyd}}\right)^2$ [*Schmitt et al.*, 2011]. Compared to many simulations shown in *Schmitt et al.* [2011], the simulations in this work are always unfavorable for thermal pressurization to dominate during quasi-static (that is, subseismic) slip speeds because d_c is smaller by a factor of 5 and $h = 50$ μm instead of zero.

In Figure 4a, both terms of equation (19) are plotted for sample high-stress and low-strength simulations during the quasi-static slip phase (up to $v_{max} \approx 0.04$ m/s). At each value of v_{max}, the values shown in Figure 4 correspond to the x coordinate with maximum $-\dot{\tau}$ (the jagged character of the lines arises from migration in x). Since the corresponding $-f_0\dot{p}$ and $\dot{f}\bar{\sigma}$ lines never intersect, no v_{crit} is defined during the quasi-static nucleation phase. For both high-stress and low-strength simulations, thermal pressurization contributes a small but significant portion (~5–10%) of the local fault weakening at $v_{max} = 0.04$ m/s. Transient pore pressures are shown in Figure 4b. Compared to the nominal effective normal stress $\bar{\sigma}$ (126 MPa in this case), values of Δp at the end of the nucleation phase are modest. Thermal pressurization is stronger in high-stress nucleation, yielding a pore pressure transient about 5 times greater than that for low-strength nucleation. This result is to be expected since $\dot{p} \propto f_0\bar{\sigma}v$.

4. Transition to Dynamic Rupture

Figure 5 shows snapshots taken from both the quasi-static and dynamic phases of the simulations of section 3.2. The nucleation phase exhibits the characteristic bilaterally growing slip pulse behavior of slip law nucleation, with only one of the slip pulses accelerating to instability [*Ampuero and Rubin*, 2008]. The width of the quasi-static slip pulse is a few L_b, where $L_b = \mu d_c / b\sigma_{eff}$. By the end of the nucleation phase, slip of 10–30 d_c occurs within the faster quasi-static slip pulse, resulting in a pore pressure transient of a few megapascals. That nucleation pulse becomes the site where dynamic rupture initiates.

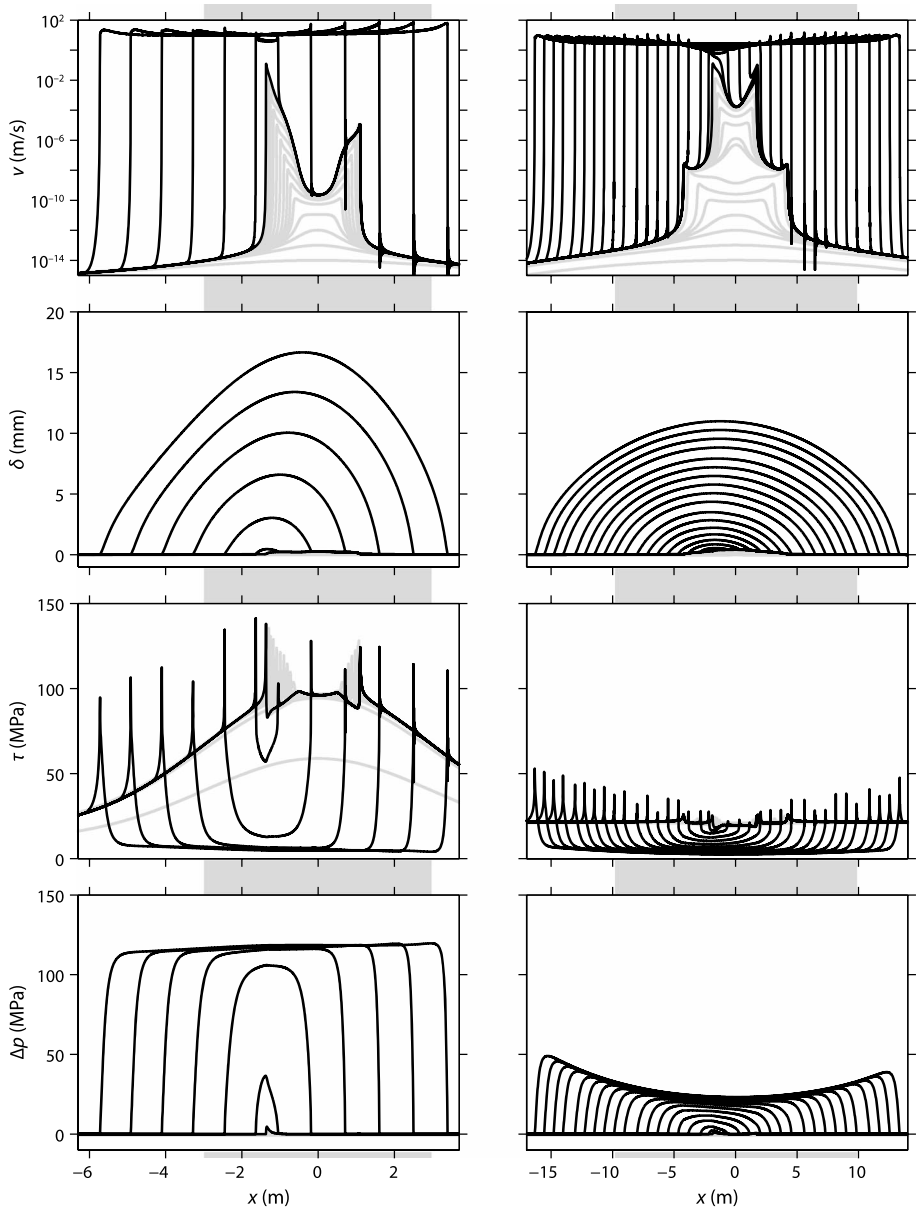

Figure 5. Transition from nucleation to dynamic rupture. (left column) A sample high-stress simulation and (right column) a sample low-strength simulation. Gray lines are snapshots during the quasi-static nucleation phase corresponding to tenfold increases in v_{max}. Black lines are snapshots at a 0.3 ms interval during the dynamic phase. The gray bars in the horizontal scales indicate the range between $\pm w$.

Dynamic rupture grows bilaterally from the nucleation site. As slip accelerates, the elastic interaction becomes increasingly significant in the equation of motion (6). Above slip speeds of $v \approx 2c_s\sigma_{\text{eff}}(b-a)/\mu$, radiation damping dominates rate/state weakening, prohibiting continued acceleration and promoting expansion of the slip zone. Since slip continues at the nucleation site for some time, the early phase of dynamic rupture is crack-like. Crack-like behavior early in dynamic rupture occurs in all of our simulations, even though nucleation is pulse-like and subsequent dynamic rupture may become pulse-like. Since dynamic rupture initiates at the tip of the nucleation slip pulse, one side (in Figure 5, the $-x$ side) of the rupture immediately enters the low-τ_{bg} zone. In the other direction ($+x$), the rupture enters a region with stress conditions favorable for slip ($\tau/\bar{\sigma} \approx f_0$ there since the fault has reached steady state) and the rupture propagates easily. At the high slip speed of dynamic rupture, thermal pressurization becomes the dominant weakening mechanism and causes a substantial decline in τ within the slip zone, which is visible in the snapshots of τ and p in Figure 5.

Following high-stress nucleation, the stress drop inside the rupture is large ($\sim\tau_0$), which corresponds with large slip and thus high slip speeds of 10–100 m/s. For low-strength nucleation, the dynamic stress drop is small and slip speeds are therefore much lower, with values of 1–10 m/s (Figure 5, top row). The relatively smaller values of v following low-strength nucleation result in weaker thermal pressurization inside the nucleation zone compared to high-stress nucleation.

The effect of nucleation (high-stress versus low-strength) persists as rupture propagates outside of the nucleating stress heterogeneity. The larger slip speeds following high-stress nucleation result in a larger concentration of stress ahead of the rupture tip. This is caused by the friction law, in which the peak stress after an increase in velocity from v_1 to v_2 is $\tau_{peak} = \tau_0 + a\bar{\sigma}\ln(v_2/v_1)$. With slip occurring at high v and an ensuing large peak-to-breakdown strength drop behind the tip, ruptures initiated at a high-stress heterogeneity therefore have strong thermal pressurization at all times during the rupture. The low-strength simulation shown in Figure 5 shows a growing Δp transient as slip propagates. As this particular rupture grows, Δp will approach the magnitude of Δp from the high-stress simulation, suggesting that some distance away from the nucleation zone the rupture tip mechanics will become similar in the two simulations. The ruptures in some simulations, however, decay as they propagate, and we explore the variability of that behavior below.

5. Rupture Sustained by Thermal Pressurization

A consequence of nucleation at a stress heterogeneity is that shear stress outside the nucleation zone τ_{bg} is so low that a considerable stress increase at the rupture tip is required for significant slip to occur. As described in section 4, dynamic slip within the nucleation zone can yield a rupture with a large stress concentration in front of the rupture and high slip speed v at its tips. Figure 6 shows how thermal pressurization sustains this condition as rupture propagates into regions of low τ_{bg}. In Figure 6a, the shear stress concentration ahead of the rupture is visible; there the entire increase in τ is accommodated by the friction coefficient since σ_{eff} remains unchanged. In Figure 6b, $\dot{f}$ is dominated by direct velocity strengthening ahead of the tip, showing that no state evolution occurs there. When v becomes sufficiently high, thermal pressurization becomes a significant weakening mechanism at and behind the rupture tip. A precipitous drop in σ_{eff} ensues and results in a large strength drop, which sustains the large jump in slip speed moving forward. Interestingly, rate- and state-dependent friction never becomes a significant weakening effect (Figure 6b, right) because thermal pressurization so strongly dominates fault weakening that slip accelerates with state evolution unable to keep up with the direct rate-strengthening effect.

Behind the rupture tip, fault strength transitions from being dominated by thermal pressurization to being controlled by the balance of diffusion and thermal pressurization. Immediately behind the rupture tip, slip speed v continues to increase along with $\dot{p}$ but only briefly until a maximum slip speed v_{max} is attained (and whose value is directly dependent on the elastic interaction). During that time, slip $\delta \gg d_c$ occurs rapidly and the fault quickly reaches steady state ($S = 0.5$ and $\ln v\theta/d_c = 0$). After reaching v_{max}, slip speed undergoes a gradual decline roughly tenfold in magnitude, which amounts to a negligibly increasing friction coefficient (dependent on the steady state friction response). Since slip continues at low τ, thermal pressurization is weak and diffusive transport decreases p, causing a gradual increase in τ; the effect is visible in Figure 6a. In Figure 6b (left), it is clear that the declining pore pressure is the dominant restrengthening mechanism inside the rupture.

In the simulation shown in Figures 6a and 6b, slip inside the rupture eventually halts and the rupture is therefore pulse-like. In this case, v and p decrease in a feedback cycle until v approaches zero. In order for the rupture to be sustained, it must always release strain energy, so restrengthening at the pulse tail must lead to a final shear stress $\tau < \tau_0$ away from the nucleation zone. Behind the pulse, pore pressure diffusion continues, but the final value of τ is achieved quickly. Since τ is fixed but σ_{eff} increases, friction responds via a large drop in θ to far below steady state, which is shown by the decline of S in Figure 6a.

Figures 6c and 6d show the alternative outcome of the v-p interaction behind the rupture tip, in which v remains sufficiently high that diffusion is unable to reduce p significantly. In this case, the fault reaches a steady state in which the thermal pressurization rate $\Lambda\dot{T}$ balances diffusive transport $c_{hyd}\mathrm{d}^2p/\mathrm{d}y^2$ and $\dot{p} \approx 0$. In the absence of other perturbations to τ or v, slip therefore continues indefinitely inside the rupture and it is crack-like. In an infinite medium, such a rupture would also grow indefinitely; the rupture propagation will continue to extract strain energy to balance the work of additional fault slip. The rates of change of fault

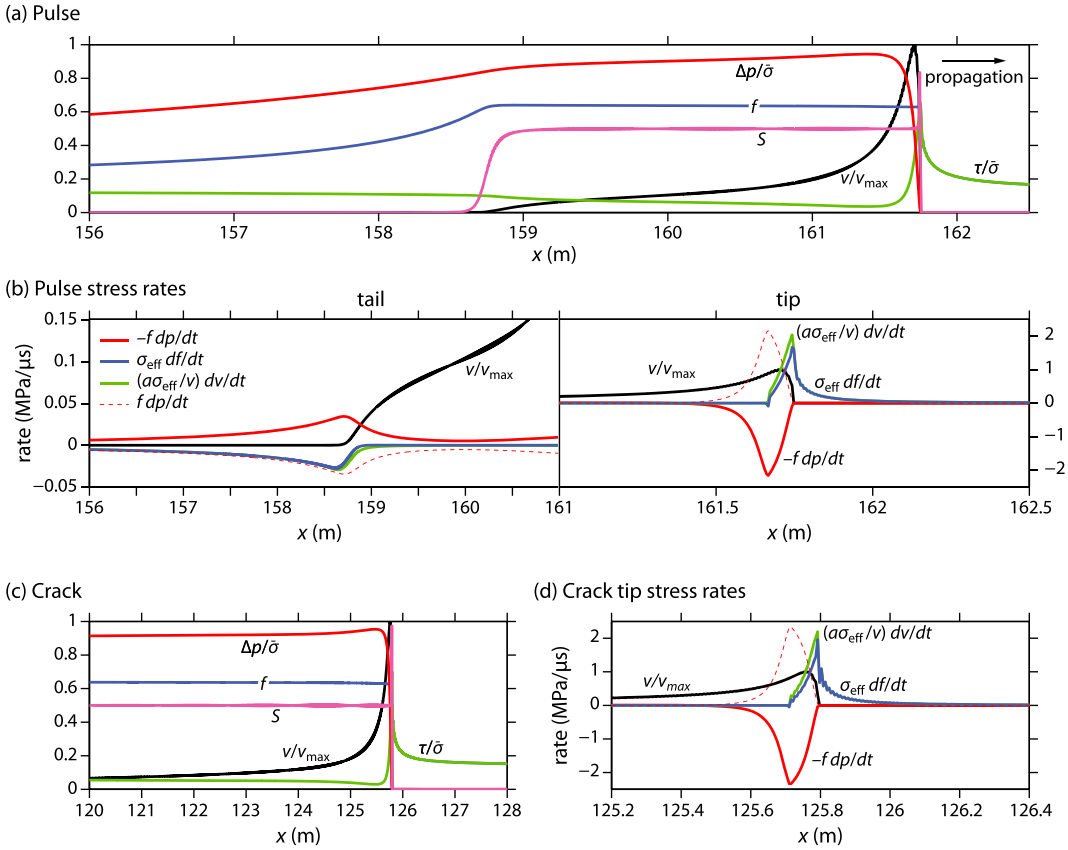

Figure 6. Evolution of stress, slip speed, and frictional state in a propagating rupture. (a) Pulse-like rupture. (b) Rates of change in a pulse-like rupture at the (right) tip and (left) tail. Dashed line is $f\dot{p}$, shown to facilitate comparison with the strengthening rates. (c) Crack-like rupture. (d) Rates of change in a crack-like rupture.

strength terms at the rupture tip in Figure 6d are qualitatively similar to those of the slip pulse of Figure 6b, which suggests that the conditions for the two modes of rupture differ only subtly.

6. Sample Numerical Simulations

As indicated in section 5, thermal pressurization is capable of sustaining rupture far outside of the stress heterogeneity where slip nucleates. In some cases, the ruptures are sustained for a finite time and then arrest, while in others the ruptures are sustained indefinitely. Section 5 also introduced pulse-like and crack-like slip sustained by thermal pressurization. Here we present output of six sample simulations for both high-stress and low-strength nucleation.

6.1. Arresting Rupture After High-Stress Nucleation

Figure 7 shows a sample arresting high-stress simulation with $\tau_{bg}/\bar{\sigma} = 0.114$ and $w = 5L_{min}$. Dynamic rupture initiates inside the nucleation zone and propagates bilaterally at nearly the shear wave speed while still in the vicinity of the stress heterogeneity. At first, the rupture is crack-like, with slip continuing across the entire region between the rupture tips. As the rupture expands away from the nucleation zone into the low-τ_{bg} region, propagation slows slightly (but remains dynamic) and an arrest front develops. Arrest first occurs over a broad portion of the interior of the rupture zone and then propagates outward toward the rupture tips, causing the rupture to take the form of a slip pulse. The healing front has an apparent velocity greater than c_s, suggesting that restrengthening is a local effect rather than a wave-mediated process. Eventually, the pulse width decays to zero and fast slip ends.

Outside of the nucleation zone, the rupture restrengthens to a final shear stress $\tau > \tau_{bg}$ (that is, the stress drop is locally negative), which is accomplished via stress transfer from the nucleation zone where the stress drop $\Delta\tau$ is large. Figure 7d shows the transient pore pressure p; because slip occurs at high stress inside the

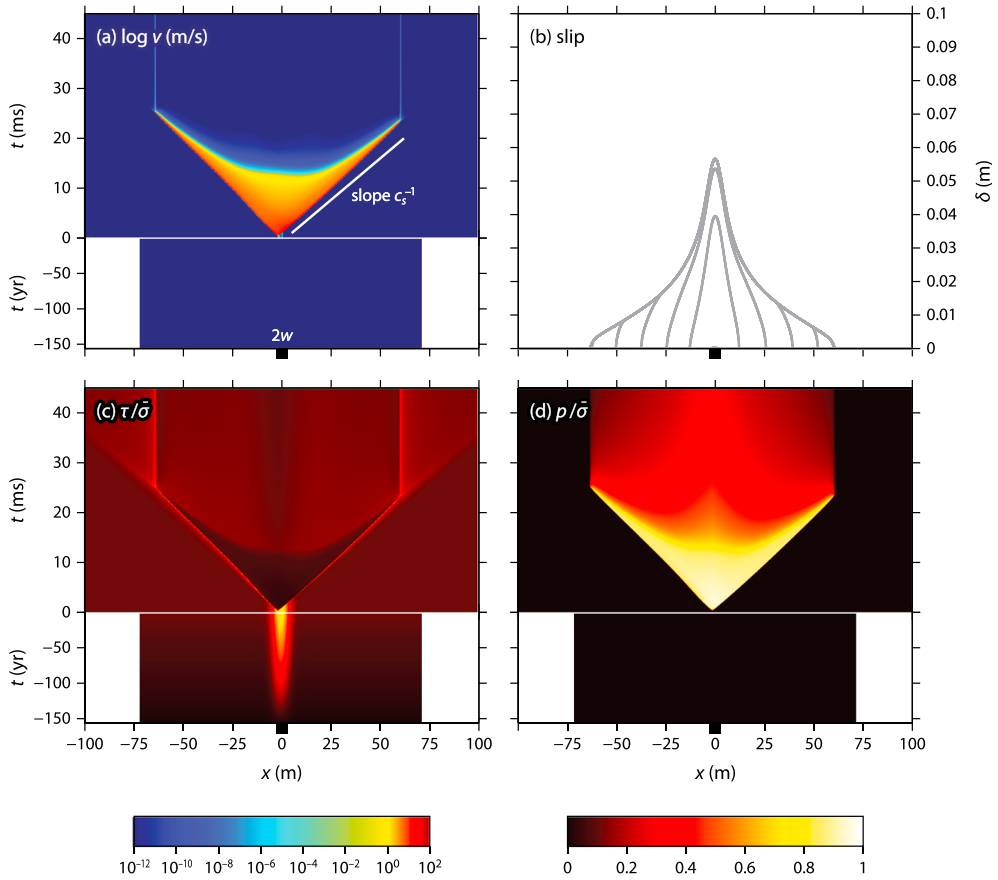

Figure 7. An arresting rupture following high-stress nucleation. (a) Space-time plot of log v. The horizontal line separates the nucleation timescale in years from the earthquake time in milliseconds. Gaussian heterogeneity width $2w$ is indicated with the black bar. The white reference line has slope c_s^{-1}. (b) Snapshots of slip every 5 ms. (c) Space-time plot of τ. (d) Pore pressure transient resulting from thermal pressurization.

nucleation zone, thermal pressurization is dramatic early in the rupture—exceeding 90% of $\bar{\sigma}$. The high slip velocity v sustains substantial thermal pressurization even as rupture propagates far from the nucleation zone. After the rupture fully arrests, diffusion rapidly reduces the transient pore pressure (Figure 7d) and temperature (not shown) anomalies.

6.2. Sustained Slip After High-Stress Nucleation

At slightly higher levels of τ_{bg} than those shown for the arresting rupture, slip pulses apparently continue indefinitely. In the simulation shown in Figure 8, $\tau_{bg}/\bar{\sigma} = 0.132$, but all other parameters are kept identical to the nominal values used throughout this paper. Initially, rupture proceeds in a similar fashion to the arresting pulse shown in Figure 7, with an early crack-like phase that undergoes widespread arrest and then forms bilaterally propagating slip pulses. In this rupture, however, the pulse appears to reach a steady state that is capable of propagating indefinitely (it is admittedly unclear if this particular rupture would ultimately arrest after a much longer time than we simulated).

Compared to the quickly arresting rupture of Figure 7, slip evolution is nearly identical inside the nucleation zone. However, as the rupture propagates into the low-τ_{bg} area, the slip at the rupture tip is at slightly higher τ since friction's direct effect results in a shear stress of roughly $\tau_{bg} + a\bar{\sigma}\ln(v/v_{init})$. The slightly higher stress at the rupture tip enhances the rate of thermal pressurization (proportional to τv), which in turn yields a slightly larger stress decrease behind the rupture tip. The larger dynamic stress drop results in slightly larger v, which also enhances thermal pressurization. The magnitudes of the v and τ differences at tips of arresting and sustained ruptures turn out to be subtle, which is apparent in the similarity of Figures 6b and 6d.

Crack-like rupture requires only slightly higher τ_{bg} than is necessary for a sustained pulse. The simulation shown in Figure 9 has $\tau_{bg}/\bar{\sigma} = 0.147$, which is only 11% higher than the condition for the sustained pulse

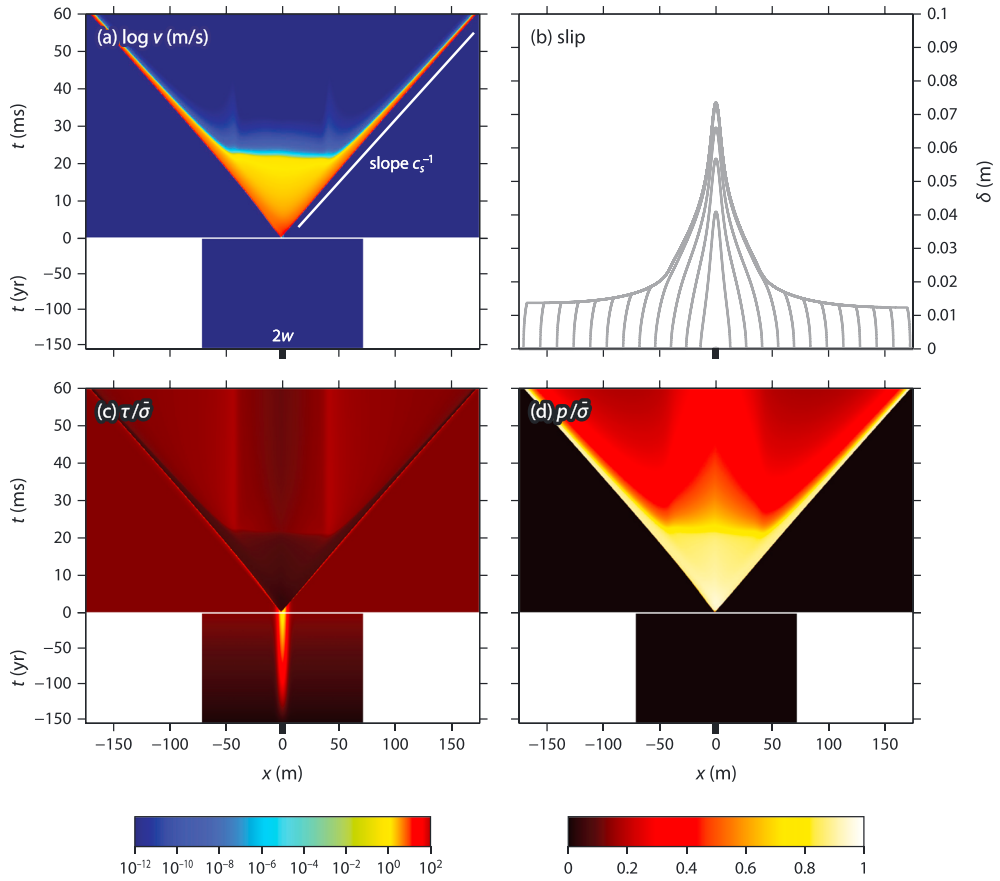

Figure 8. A high-stress simulation with a sustained slip pulse.

of Figure 8. Again, slip evolution within the nucleation zone is nearly identical to that of the lower-τ_{bg} examples, but the rupture results in qualitatively different behavior as it propagates through the low-τ_{bg} region. Further-enhanced thermal pressurization at the rupture tip allows for sustained crack-like rupture like that shown in Figures 6c and 6d. Since thermal pressurization and diffusion balance each other inside the crack, the pore pressure remains high and the shear stress remains low. Compared to the arresting and pulse-like ruptures, the propagation speed is also faster (99.5% of c_s in this example, versus 96% and 98.5% in the former examples).

6.3. Arresting Rupture After Low-Strength Nucleation

Figure 10 shows a sample low-strength simulation, which is qualitatively different from the high-stress arresting rupture of Figure 7 in that rupture arrests from the tips inward rather than from the nucleation zone outward. In this simulation, $w = 4L_{min}^{LS}$ and $\tau_{bg}/\sigma_{eff} = 0.130$—a background stress state nearly identical to the sustained pulse resulting from high-stress nucleation (Figure 8). Clearly, differences in the nucleation process affect rupture evolution. Compared to high-stress rupture, the early dynamic stress drop is smaller because initial shear stress in the nucleation zone is much lower, and slip speed v is consequently lower as well. The relatively weak early phase of rupture (low τ, low v, and small $\Delta\tau$) is thus unfavorable for thermal pressurization as the tip propagates away from the stress heterogeneity. However, mild thermal pressurization does support continued slip weakening in the interior of the rupture.

With further propagation, thermal pressurization grows in intensity (Figure 10d) but fails to sustain rupture growth. After the rupture tip propagates a few stress heterogeneity widths w in both directions away from the nucleation zone, thermal pressurization stalls and the rupture stops growing. Stopping phases emanate from both rupture tips and propagate inward from both tips at a velocity slightly below c_s, which contrasts to the local diffusive restrengthening that arrests slip in high-stress ruptures. Figure 10c shows that τ increases after the passage of the arrest wave but that increase is attributed to the reduction of radiation damping corresponding to abrupt deceleration of slip. The stress interaction $\psi(x, t)$ is in fact negative valued following

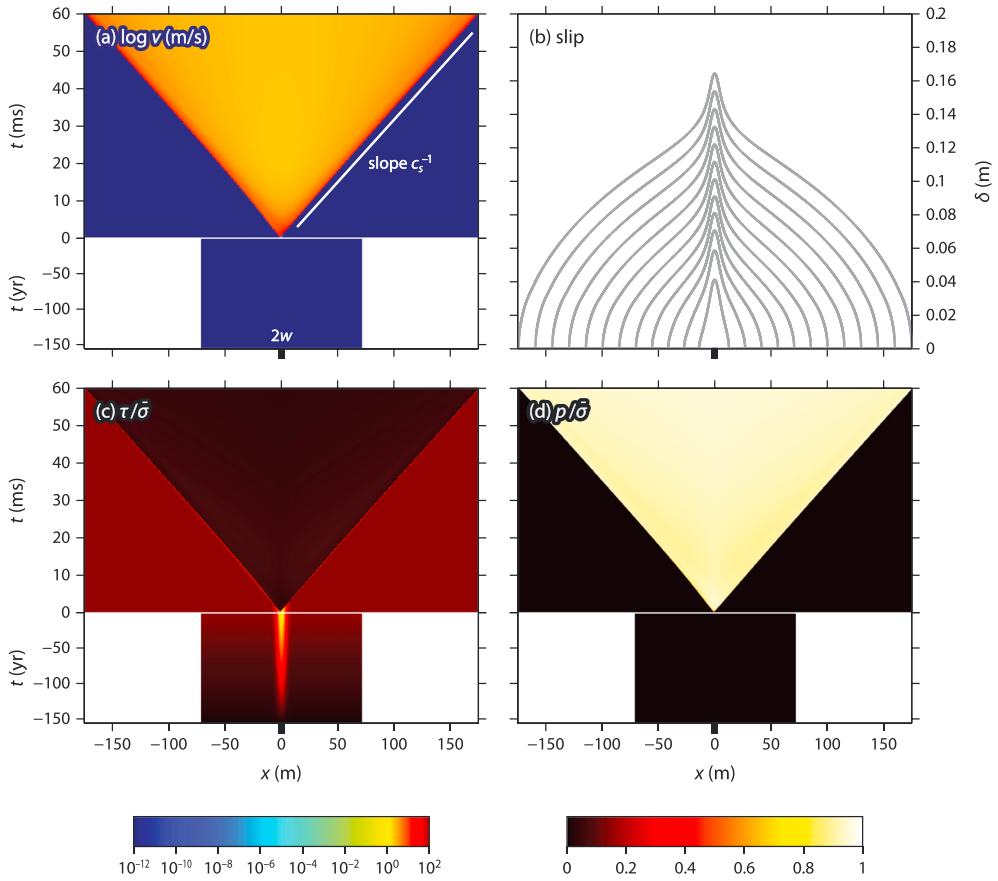

Figure 9. A high-stress simulation with a sustained crack-like rupture.

the passage of an arrest wave; interestingly, the superposition of the two stopping phases in the center of the rupture drives shear stress below zero and reverse slip occurs (Figure 10c).

6.4. Sustained Slip After Low-Strength Nucleation

As shown above, even though low-strength nucleation yields modest thermal pressurization inside the nucleation zone, the effect grows in intensity as rupture proceeds (Figure 5 and even in Figure 10d before arrest begins). Figure 11 shows a simulation with $\tau_{bg} = 0.17\bar{\sigma}$, in which sustained rupture occurs. As rupture propagates away from the nucleation zone, thermal pressurization becomes comparable in magnitude to that of Figure 9. Early in the dynamic rupture, growing thermal pressurization at the rupture tip leads to a growing $\Delta\tau$, which in turn leads to increased v at the tip, completing the feedback loop described in section 5. Since high-v, high-τ slip never occurs inside the nucleation zone, Δp remains low there (Figure 11d) but slip continues because modest thermal pressurization allows for ongoing weakening.

Pulse-like ruptures can occur following low-strength nucleation, but they are unlike the high-stress example shown in Figure 8. In this case, prolonged slip inside the low-strength heterogeneity prevents diffusion from establishing a restrengthening pulse tail, so pulses arise out of a more complicated elastic interaction that is effectively the combination of the arrest process of Figure 10 and the sustained rupture of Figure 11. With an intermediate value of $\tau_{bg} = 0.15\bar{\sigma}$ between the preceding examples, the simulation of Figure 12 exhibits such a pulse-like behavior. Dynamic rupture nucleates at the left side of the nucleation zone. In the $+x$ direction, the rupture propagates back through the nucleation zone, where the fault is at steady state and is primed for frictional weakening with further slip. The rupture attains sufficient slip speeds to sustain thermal pressurization, and the rupture tip is thus able to propagate indefinitely. In the opposite ($-x$) direction, however, the rupture tip enters a region far below steady state, and the peak slip speed at the rupture tip is slightly lower. Thermal pressurization is unable to sustain rupture in that direction, and arrest occurs in the same manner as in section 6.3. Hence, an "arrest wave" follows the rupture tip, producing a slip pulse, an arrest mechanism first

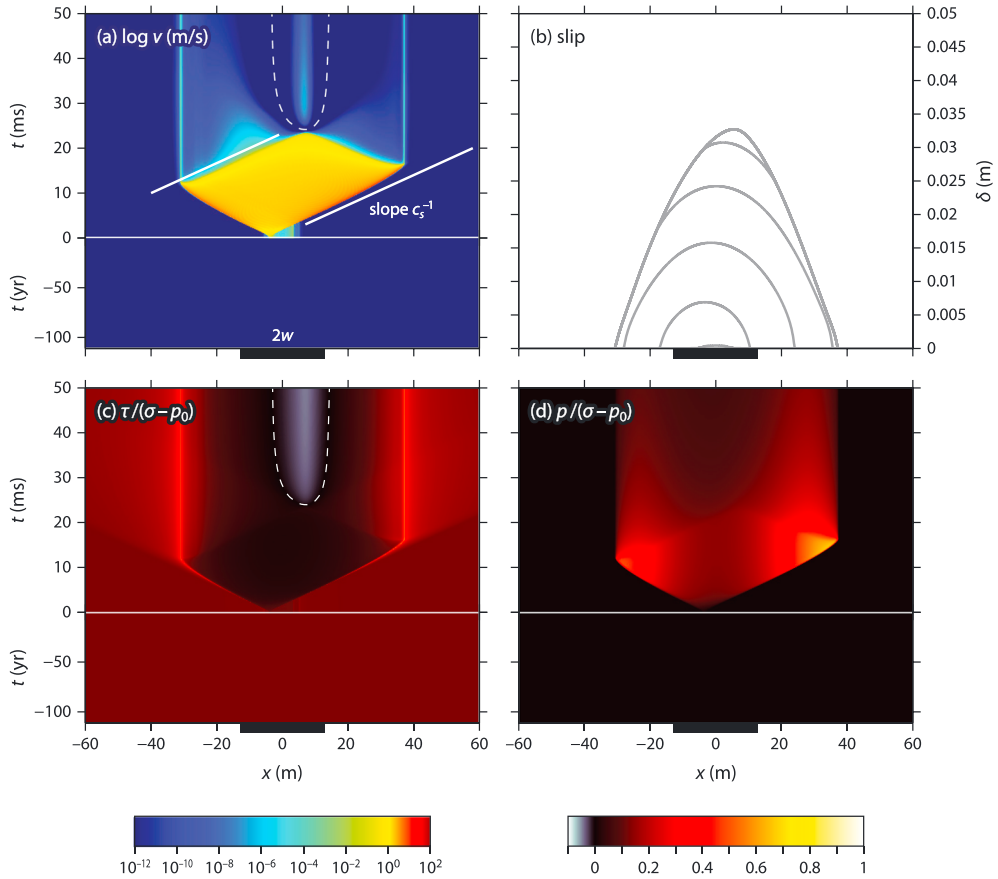

Figure 10. A low-strength simulation with an arresting rupture. Reverse afterslip occurs in a central portion of the rupture zone where τ changes sign, marked with a dashed line.

identified by *Johnson* [1990]. In this case, the pulse width is controlled by the runout distance of the arresting tip, rather than the interaction of diffusion with rupture propagation.

7. Discussion

7.1. Conditions for Sustained Rupture

While our simulations shared identical material properties, we varied the width of the nucleation zone w and the background shear stress τ_{bg} to explore their effects on rupture mode. Figure 13 summarizes results from all of our simulations. Consistent with prior studies that include dynamic weakening mechanisms [e.g., *Cochard and Madariaga*, 1994; *Zheng and Rice*, 1998; *Noda et al.*, 2009; *Gabriel et al.*, 2012], low values of τ_{bg} result in arresting ruptures and high values of τ_{bg} result in sustained, crack-like ruptures. Additionally, the width of the nucleation zone w also affects the rupture mode, with larger w favoring sustained ruptures. This is likely a consequence of wider ruptures having larger-amplitude stress concentrations ahead of the rupture tip when the rupture exits the nucleation zone. That larger stress at the rupture tip both contributes directly to increased thermal pressurization (since $\dot{p} \propto \tau v$) and leads to larger slip speeds at rupture tips via the direct effect of rate- and state-dependent friction. However, *Gabriel et al.* [2012] observe similar behavior in models where the dynamic weakening occurs because of the friction law.

Sustained slip pulses (as shown in Figures 8 and 12) occur in both high-stress and low-strength models but only in a small parameter space between arresting ruptures and sustained cracks. With a different fault constitutive relationship and artificially imposed nucleation, *Gabriel et al.* [2012] observed that the τ_{bg} range that accommodates sustained pulses grows with increasing nucleation zone size; computational limitations prevented us from testing if that behavior occurs with thermal pressurization. All pulses observed were consistent with those described in section 6, in that the shear stress recovery in high-stress slip pulses was self-healing

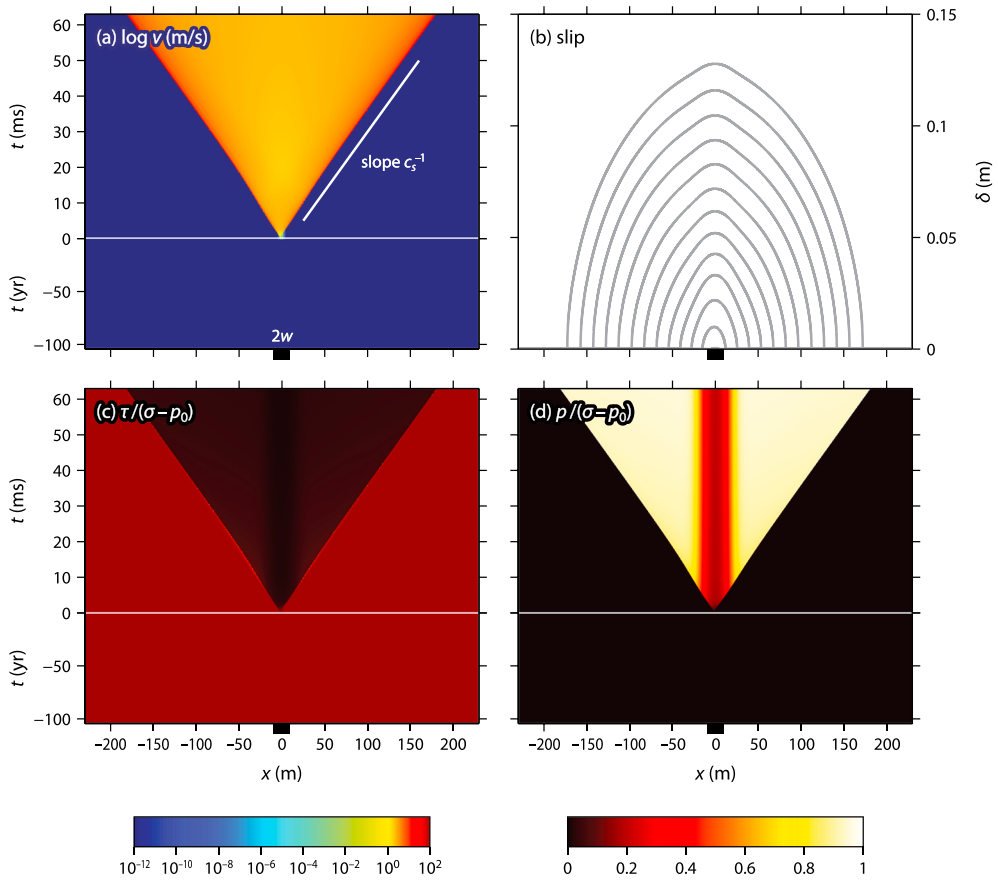

Figure 11. A low-strength simulation with sustained crack-like rupture.

due to diffusion, while dynamically propagating elastic arrest waves induce restrengthening to form slip pulses in low-strength models.

We are unable to provide an expression capable of predicting the τ_{bg} threshold for sustained rupture. *Zheng and Rice* [1998] proved that for spatially uniform frictional behavior, crack-like ruptures require that the condition $\tau(v) \leq \tau_0 - \mu v/(2c_s)$ be satisfied for some v, where τ_0 is the initial shear stress. For constitutive models in which shear resistance τ is a unique function of slip speed v, a minimum shear stress capable of sustaining a crack can therefore be defined by finding the smallest value of τ_{bg} ($= \tau_0$ for $|x| \gg w$) for which the condition can be true. Lower values of τ_{bg} require ruptures that either arrest or take the form of a pulse. This approach works satisfactorily for rate- and state-dependent friction because slip inside the rupture is at steady state (and follows equation (12)). However, the introduction of thermal pressurization causes τ to depend on slip history as well as current slip speed, and the approach of *Zheng and Rice* [1998] then cannot be used to determine a τ_{bg} threshold for crack-like rupture for thermal pressurization.

7.2. Earthquake Source Parameters

For arresting ruptures, we may extract values from the simulations to compare with source parameters inferred for natural earthquakes. Such a comparison is imperfect; our simulations are in a 2-D medium, while natural earthquakes have an additional spatial dimension. Further, simulations yield actual values of physical parameters: rupture half-length R, slip $\delta(x)$, moment M_0, moment rate function $\dot{M}_0(t)$, the frictional resistance to slip $\tau(x)$, and the total change in strain energy E_W. For natural earthquakes, these values are inferred from seismograms via models based on several assumptions (such as slip distribution, seismic wave takeoff angle, and path effects) and typically require a large data set to be capable of giving a picture of earthquake source physics.

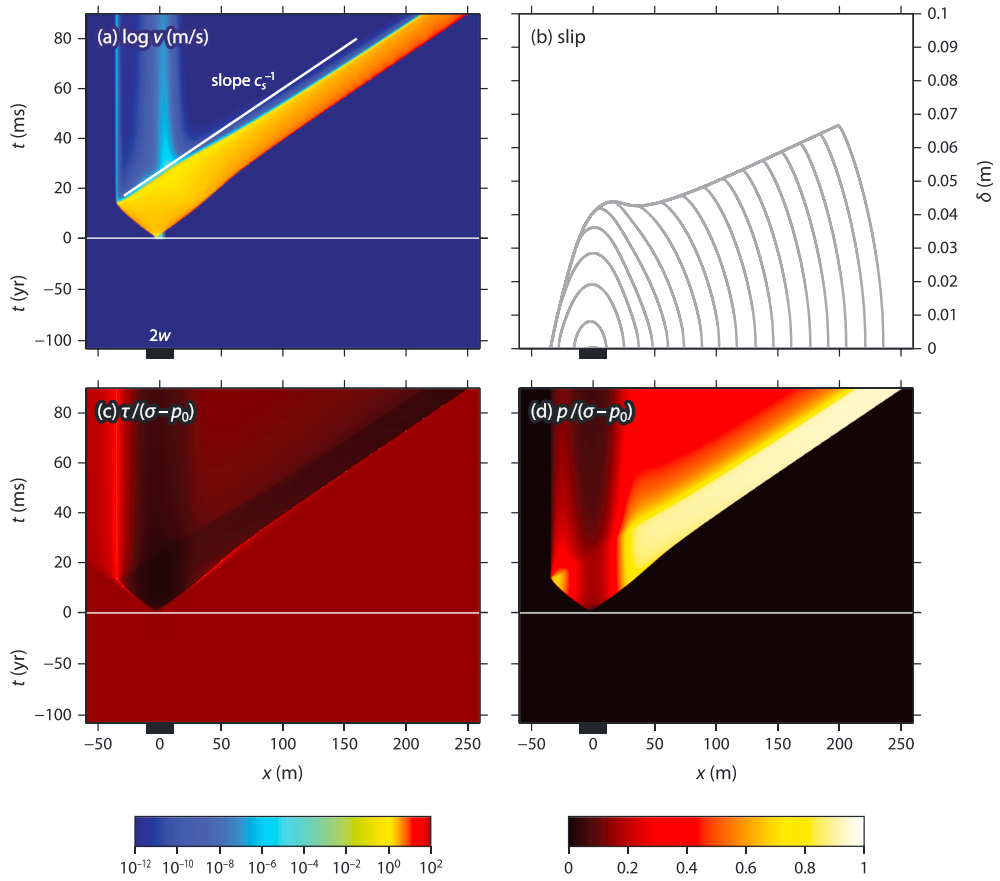

Figure 12. A low-strength simulation with a sustained slip pulse.

7.2.1. Rupture Length and Seismic Moment

In our simulated ruptures, both half-length R and seismic moment M_0 depend on background shear stress and nucleation zone size. We define half length as

$$R(t) = \frac{x^+_{\text{prop}}(t) - x^-_{\text{prop}}(t)}{2}, \tag{20}$$

where $x^-_{\text{prop}}(t)$ and $x^+_{\text{prop}}(t)$ indicate the tip positions of each side of a bilaterally propagating rupture. Seismic moment is similarly defined as

$$M_0(t) = \mu \int_{x^-_{\text{prop}}(t)}^{x^+_{\text{prop}}(t)} \delta(x,t)\, \mathrm{d}x\,, \tag{21}$$

where δ is slip. Since our simulations are in 2-D, M_0 has units of moment per unit fault width. Figure 14 shows how final values R and M_0 relate to τ_{bg} and w for all simulations in which rupture arrests. The most significant difference between the two nucleation regimes is that high-stress nucleation has smaller minimum R and M_0 because $L_{\text{min}} \propto \bar{\sigma}^{-1}$, and $\bar{\sigma}$ is larger inside the nucleation zone in the high-stress case. In general, ruptures have larger R and M_0 as either τ_{bg} or w increases. In the low-strength case, Figure 14 obscures that relationship because simulations are grouped by w/L_{min} value and $L^{\text{LS}}_{\text{min}} \propto \tau_{\text{bg}}^{-1}$ in the low-strength case; lines are drawn to emphasize the actual dependence on τ_{bg}.

To highlight differences in how thermal pressurization extends rupture in the two loading regimes, we consider a normalized runout distance away from the nucleation zone $(R-w)/w$ in Figures 14c and 14d. We also indicate the lowest τ_{bg} value resulting in sustained crack-like rupture for each family of simulations. Sustained rupture occurs at slightly higher values of τ_{bg} than the largest arresting ruptures (see also Figure 13), which indicates that the transition from arresting to sustained rupture is abrupt. For arresting high-stress ruptures, the enhanced early thermal pressurization allows them to propagate far into the low-τ_{bg} region, with $R \approx 4w$ even as τ_{bg} approaches zero. It is likely for high-stress ruptures that all values of $(R-w)/w > 3$ are possible for

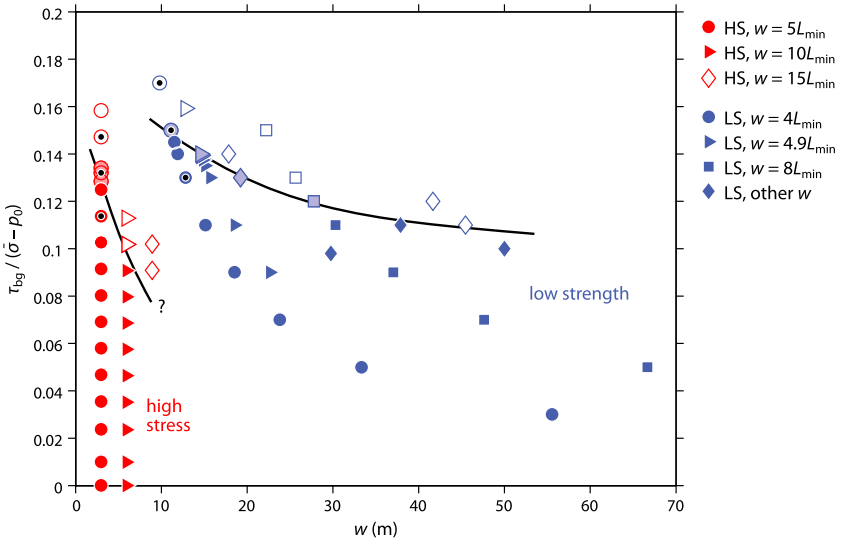

Figure 13. Variability of rupture mode depending on background shear stress τ_{bg} and nucleation zone width w. Red symbols are for high-stress simulations, and blue symbols are for low-strength simulations. Open symbols indicate sustained crack-like rupture, lightly shaded symbols indicate sustained slip pulses, and solid symbols indicate arresting ruptures. Symbol shapes correspond to families of simulations with identical w/L_{min}, except for diamonds, which have various values of w/L_{min}. The six simulations shown in Figures 7–12 are marked with black dots. Sustained slip pulses exist in a very small parameter space (near the black lines) between sustained crack-like ruptures and arresting ruptures.

arresting ruptures but with increasing sensitivity to minute increases in τ_{bg}. Low-strength arresting ruptures, on the other hand, appear to be constrained to rupture lengths of only a few w without additional complexity in the initial stress field, given that the one-sided arrest shown in Figure 12 occurs at $x^-_{prop} = 3.1w$.

The nonunique scaling of earthquake size and moment with background shear stress and nucleating heterogeneity size in Figure 14 indicates that seismic observations of small earthquakes are unlikely to contain usable information about such fault properties if thermal pressurization is active.

7.2.2. Stress Drop

We plot the relationship between mean (spatially averaged) stress drop and moment in Figure 15a, where mean stress drop is defined as

$$\Delta\tau = \frac{1}{x^+_{prop} - x^-_{prop}} \int_{x^-_{prop}}^{x^+_{prop}} [\tau_0(x) - \tau(x, t_R)]\, dx\,, \tag{22}$$

evaluated at time t_R when slip has everywhere effectively stopped. Shear stress τ remains nearly constant after t_R, which is visible in Figures 7c and 10c. While high-stress and low-strength ruptures have comparable magnitudes of $\Delta\tau$, the scaling with M_0 differs. Small-M_0 ruptures occur mostly within the nucleation zone, where the loading stress is high in high-stress ruptures. Larger-M_0 ruptures involve more of the fault outside of the nucleation zone, where τ_0 (and therefore $\Delta\tau$) is small. Thus, for high-stress nucleation, stress drop decreases with moment, for given nucleation width w. The $\Delta\tau$-M_0 relationship for low-stress arresting ruptures has a different form. Starting from extremely low τ_{bg}, increasing τ_{bg} (moving upward within a w/L_{min} family in Figure 15a) corresponds to increasing $\Delta\tau$. But as τ_{bg} approaches the threshold for sustained rupture, M_0 increases with little additional increase of $\Delta\tau$, presumably due to thermal pressurization extending rupture size. This saturation of stress drop is not surprising since $\Delta\tau < \tau_{bg}$ averaged over the fault. In both loading regimes, however, it must be noted that M_0 is strongly dependent on w while $\Delta\tau$ is only weakly dependent on w. Hence, there is no unique relationship between moment and mean stress drop for either type of rupture.

Our simulated earthquakes have mean stress drops in the range of 1–20 MPa, which is consistent with values for small earthquakes inferred from seismological observations. Seismologists [e.g., *Abercrombie*, 1995] often interpret moment-length relationships for populations of earthquakes in the framework of uniform stress-drop circular cracks [*Eshelby*, 1957]. Since our simulations are 2-D antiplane, we must use the analogous relationship, a 2-D crack with uniform stress drop. In this case, the slip distribution is

$$\delta(x) = \frac{2\Delta\tau}{\mu}\sqrt{R^2 - x^2}\,, \tag{23}$$

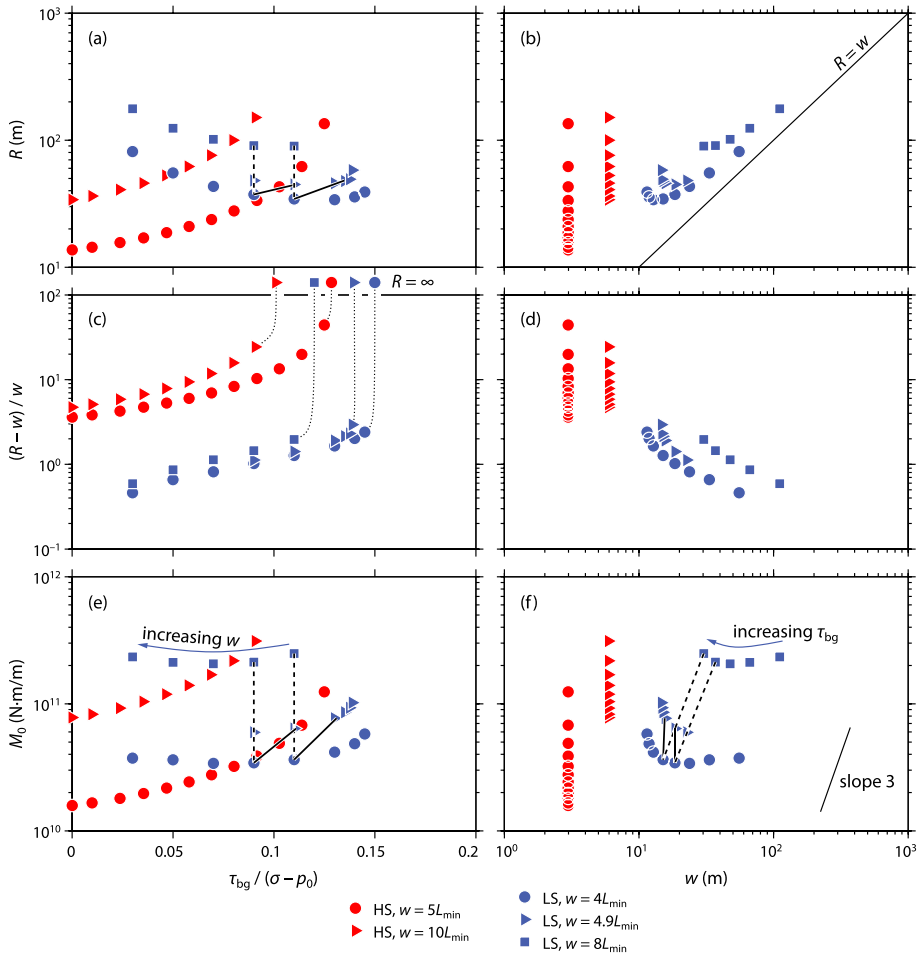

Figure 14. Rupture length and moment dependence on τ_{bg} (in Figures 14a, 14c, and 14e) and w (in Figures 14b, 14d, and 14f). Symbols correspond to families of w/L_{min} in Figure 13. Dashed lines (in Figures 14a, 14e, and 14f) group low-strength simulations that share a τ_{bg} value; solid lines group simulations that share a w value. (a, b) Rupture half-length. (c, d) Half-length normalized by nucleation zone size w. Values of τ_{bg} that lead to indefinitely sustained rupture ($R = \infty$) are shown in Figure 14c. (e, f) Moment (per unit fault width, because of the 2-D elastic medium).

which, substituted into equation (21), yields

$$M_0 = \pi R^2 \Delta\tau \,. \tag{24}$$

Using equation (24), lines of constant R are shown in Figure 15a and lines of constant $\Delta\tau$ are shown in Figure 15b. Figure 15b is a common type of plot used (with axes transposed) to present earthquake source parameters, and the lines of constant $\Delta\tau$ show graphically how stress drop is inferred. Comparing to the actual values of $\Delta\tau$ in Figure 15a, the values predicted by equation (24) are slightly higher than the actual values. It turns out that the crack model consistently overpredicts stress drop by a factor of ~1.4, which is visible in the ratios of crack model $\Delta\tau$ to actual $\Delta\tau$ shown in Figure 15c. Hence, the uniform stress-drop crack model may still be used to infer stress drops for small earthquakes that are not necessarily crack-like, but a correction factor must account for the model's overprediction of $\Delta\tau$.

In general, our simulations produce stress drops that are comparable to seismologically inferred values of 1–10 MPa. High-stress ruptures with small moment, however, have larger stress drops because of large $\Delta\tau$ in the nucleation region. Even so, mean stress drops in that case are still much lower than fault's static strength because rupture propagates into the low-τ_{bg} region. We caution, however, that direct comparison between seismologically inferred M_0-R relationships and simulation output is complicated by many assumptions that are made in obtaining R from seismograms.

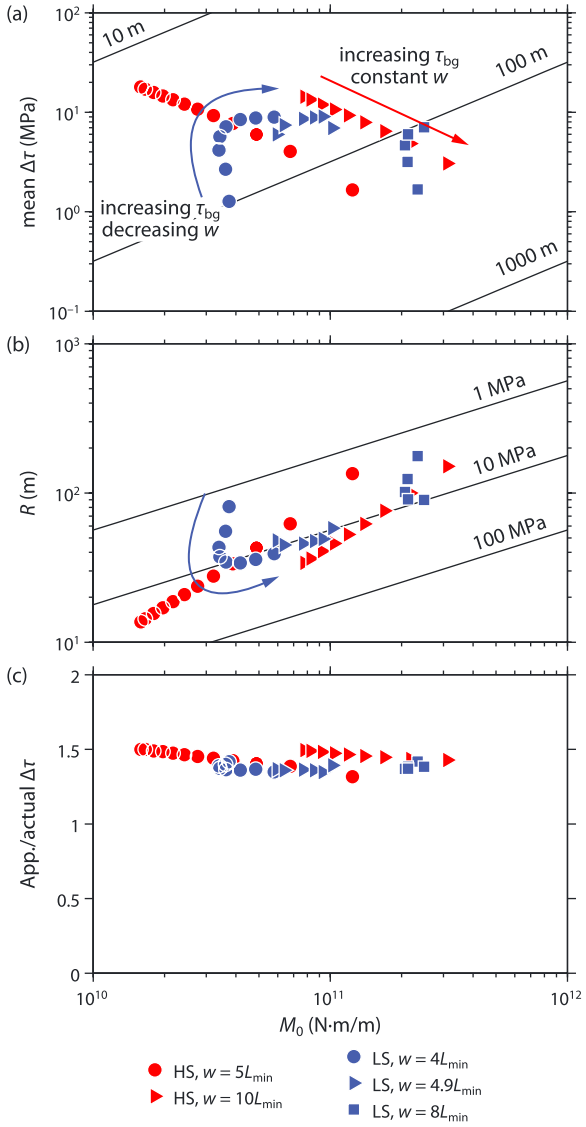

Figure 15. Relationships between stress drop and rupture size for arresting ruptures. Arrows are drawn to facilitate comparison to Figure 14. (a) Stress drops, averaged across the width of the rupture. Lines are contours of constant R from equation (24). (b) Rupture length. Lines are contours of constant $\Delta\tau$ from equation (24). (c) The ratio of the apparent stress drop from Figure 15b to the actual stress drop shown in Figure 15a.

7.2.3. Moment Rate and Event Duration

High-strength and low-stress models differ in their initial moment release during seismic rupture. In Figure 16a, moment rate $\dot{M}_0(t)$ is plotted for all of our simulations. Moment rate is the time derivative of equation (21), which is simply

$$\dot{M}_0(t) = \mu \int_{x^-_{prop}(t)}^{x^+_{prop}(t)} v(x,t)\, dx\,. \tag{25}$$

To compare the early growth rate of M_0, we measure its timescale $M_0/\dot{M}_0$ evaluated when $\dot{M}_0 = 10^{12}$ N m/m/s (Figure 16b). Smaller values of $M_0/\dot{M}_0$ correspond to more impulsive rupture growth. A uniform stress case in which the entire fault is critically loaded yields the maximum growth of M_0 and $\dot{M}_0$ for a given value of $\bar{\sigma}$. High-stress ruptures initiate equally impulsively since the stress state in the nucleation zone is similar to that of the uniform τ model. As rupture propagates into the low-τ_{bg} region, however, $\dot{M}_0$ grows more slowly. Larger nucleation zone size w therefore corresponds to a longer duration of impulsive rupture growth. For pulse-like high-stress ruptures, $\dot{M}_0$ declines as slip inside the nucleation zone stops and the slip pulse develops. The decay of $\dot{M}_0$ can last for a long time compared to the initial impulsive rupture of the nucleation zone.

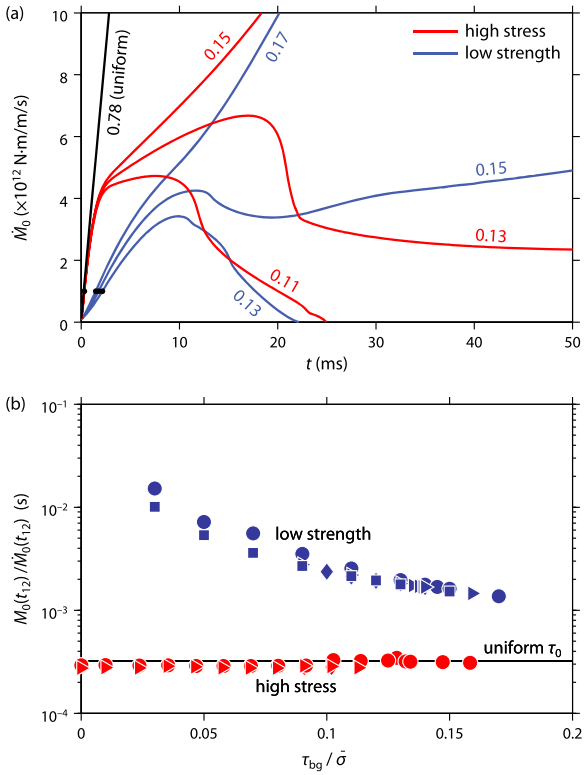

Figure 16. (a) Sample moment rate functions for the sample ruptures shown in Figures 7–11, as well as for a simulation with uniform τ. Values of $\tau_{bg}/\bar{\sigma}$ at the initiation of seismic slip are indicated. (b) Evolution timescale for early M_0, defined as $M_0/\dot{M}_0$ at time t_{12} when $\dot{M}_0 = 10^{12}$ N m/m/s (marked with black dots in Figure 16a).

Low-strength ruptures, on the other hand, initially rupture less impulsively with more subdued growth of $\dot{M}$, despite the fact that the slip zone is spatially larger. The reduced early $\dot{M}_0$ is a consequence of much lower slip speeds inside and near the nucleation zone. Since low-strength ruptures that arrest tend to do so by stopping phases propagating inward at roughly the same speed as the initial growth (for example, Figure 10), the decay of $\dot{M}_0$ is typically at a similar rate as the growth phase.

The differences in early moment rate between the two rupture modes would be challenging to capture in seismic recordings. The principal differences between high-stress and low-strength moment rate functions occur over the first few tens of milliseconds of the rupture, which correspond to seismic radiation at frequencies above ~50 Hz. Instruments located close to such ruptures in boreholes or mines may, however, be able to detect these differences. Rupture in 3-D greatly obscures the difference between the two moment rate functions. For our simple antiplane ruptures, $\dot{M}_0$ is proportional to x_{prop} for the crack-like slip early in the rupture, but another spatial growth dimension introduces an additional factor of x_{prop} in $\dot{M}_0$. Low-strength ruptures initiate over much wider regions and therefore start with larger values of $x_{prop}(t)$, which in 3-D significantly diminish the difference in moment rate between high-stress and low-strength ruptures.

In our simulations, total rupture duration t_R most strongly depends on rupture half-length R. Since high-stress ruptures both grow and arrest outward from the nucleation zone, the rupture duration is equivalent to R divided by the mean propagation speed. Figure 17 shows rupture durations from our simulations normalized by c_s/R; values of $t_R c_s/R = 1$ correspond to ruptures that propagate at c_s until they completely arrest. Outside the nucleation zone, propagation speeds increase with τ_{bg}, which results in the decreasing values of $t_R c_s/R$ seen in the high-stress case. Low-strength ruptures, however, grow outward just below c_s and then arrest from the tips inward, also just below c_s. Hence, their durations are $t_R \approx 2R/c_s$.

One important consequence of the difference in duration between high-stress and low-strength ruptures is the suggestion that seismological methods of inferring an earthquake's size based on its displacement spectrum may yield biased estimates depending on whether ruptures arrest inward or outward. Far-field displacement waveforms are proportional to the moment rate function [*Aki and Richards*, 2002, chap. 4], and we

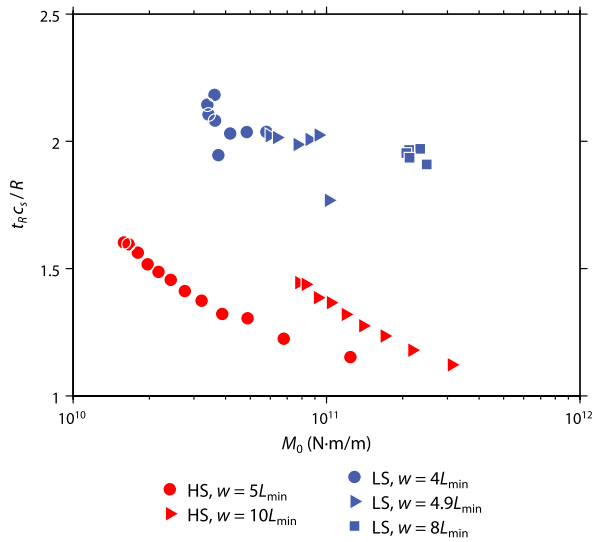

Figure 17. Normalized durations for arresting ruptures.

observe a variation of up to a factor of ~2 between durations of high-stress and low-strength ruptures of comparable moment. The protracted slip in low-strength ruptures thus contributes an additional longer-period signal that could be misinterpreted as a larger spatial extent.

7.3. Energy Budget
7.3.1. Definitions

During an earthquake strain energy release is dissipated in two ways: radiation of seismic waves and frictional work. Elasticity transfers energy across spatial dimensions, but it is instructive to first consider the work done at a given point on the fault. Figure 18 shows a schematic stress-slip curve from a rupture sustained by thermal pressurization, from which frictional work can be calculated. Prior to arrival of the stress change associated with the rupture, the initial shear stress is τ_0. As the rupture tip nears, stress increases with negligible slip. After stress increases to a peak τ_{peak} (effectively, the yield strength of the fault), slip occurs and the shear stress decreases dramatically due to thermal pressurization. The stress drops to a minimum value τ_b called the "breakdown strength" (we choose this terminology based on the concept of breakdown work from *Tinti et al.* [2005]; τ_b is often called "residual strength," which can be confusing if strength increases slightly with additional slip). While the fault is locally still slipping, diffusion and slip deceleration cause a slight increase in shear stress. For arresting or pulse-like ruptures, slip ceases at a final value δ_f at stress τ_f (which may locally exceed τ_0 in arresting ruptures).

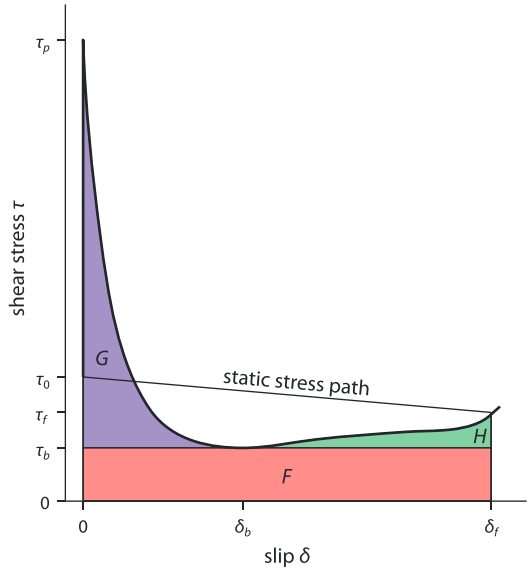

Figure 18. Sample stress-slip curve for a point on a fault as it experiences a passing slip pulse sustained by thermal pressurization. The terms *G*, *F*, and *H* are defined in equations (26)–(28).

The local frictional work can be partitioned into three terms: fracture energy, baseline frictional work, and restrengthening work. The fracture energy (actually energy per unit fault area) is the area shown in blue in Figure 18 and is defined as [*Tinti et al.*, 2005]

$$G(\mathbf{x}) = \int_0^{\delta_b} \tau(\delta) - \tau_b \, \mathrm{d}\delta \,, \qquad (26)$$

where δ_b is the "breakdown slip" corresponding to τ_b. Equation (26) represents the work done to extend the rupture at location **x**. If slip locally

arrests at final value δ_f, the baseline frictional work is simply

$$F(\mathbf{x}) = \tau_b \delta_f \,, \tag{27}$$

and the restrengthening work [*Tinti et al.*, 2005] is

$$H(\mathbf{x}) = \int_{\delta_b}^{\delta_f} \tau(\delta) - \tau_b \, \mathrm{d}\delta \,. \tag{28}$$

The sum $J(\mathbf{x}) = F(\mathbf{x}) + G(\mathbf{x}) + H(\mathbf{x})$ represents the sum of frictional work done at coordinate $\mathbf{x}$; for ruptures that arrest, the total frictional work done on the entire fault during the earthquake is

$$E_F = \int_S J(\mathbf{x}) \, \mathrm{d}S \,, \tag{29}$$

where S is the rupture area. After rupture arrests, the change in strain energy can be calculated from the equivalent quasi-static work done (per unit fault area) changing the fault from its preslipped stress state to its postrupture stress state. Graphically, the local quasi-static work at coordinate $\mathbf{x}$ is the area under the straight line in Figure 18 connecting $(0, \tau_0)$ and (δ_f, τ_f), which is

$$\Delta W(\mathbf{x}) = \frac{\tau_0 + \tau_f}{2} \delta_f \,. \tag{30}$$

While $\Delta W(\mathbf{x})$ is written here as a local quantity, its value actually depends on slip everywhere on the fault [*Rivera and Kanamori*, 2005]. The change in strain energy for the entire rupture is thus

$$E_W = \int_S \Delta W(\mathbf{x}) \, \mathrm{d}S \,. \tag{31}$$

Assuming that no other dissipative processes are active, the energy expended in seismic radiation is the difference between the change in strain energy and the frictional work done,

$$E_S = E_W - E_F \,. \tag{32}$$

The seismic energy E_S is a parameter that can be inferred from seismograms, though with considerable difficulty owing to complex wave propagation effects.

7.3.2. Fracture Energy in Simulated Ruptures

Figure 19 shows values of fracture energy $G(x)$ and local frictional work $J(x)$ for the simulations shown in section 6. Since slip continues indefinitely in the sustained crack-like ruptures, $F(x)$ and $H(x)$ are everywhere undefined for those simulations. Fracture energy $G(x)$ is also undefined since further slip leads to a reduction in τ (and therefore growth of $G(x)$). However, in the $\tau(\delta)$ relationships shown in Figure 19, a local minimum in $\tau(\delta)$ forms after slip δ_b' due to the effectively undrained thermal pressurization resulting from the early slip at high τ. After that initial stress minimum, some diffusive healing occurs before the ensuing large-δ, low-τ thermal pressurization causes additional weakening. For the crack-like ruptures shown, the initial stress minimum occurs at $\delta_b' = 0.005$ m, after which τ first increases with additional δ. Then τ declines again, reaching new minima with $\delta > 0.06$ m. The identification of τ_b and δ_b at a larger value of δ is the cause of the discontinuities in $G(x)$ for the crack-like ruptures in Figures 19a and 19c (for example, the apparent increase in G for $x < 80$ m for the high-stress crack case). The same is true for the low-strength pulse, which was shown in section 6.3 to be a crack-like rupture that is halted by an arrest wave. In those cases, the lower values of $G(x)$ at larger x reflect calculation of $G(x)$ up to the initial breakdown slip δ_b' only, since the simulations are stopped before subsequent weakening occurs.

The consistent values of $G(x)$ when prolonged slip does not occur indicate that for small earthquakes dominated by thermal pressurization, the fracture energy is controlled by nearly undrained thermal pressurization during the first increment of slip at each point on the fault. Without transport of heat and pore pressure, G initially grows rapidly with slip but approaches an upper bound as the fault fully weakens after finite slip of $\sim \delta_b$. Figure 20a summarizes the fracture energy results from all arresting simulations by comparing average fracture energy,

$$\langle G \rangle = \frac{1}{x_{\mathrm{prop}}^{+} - x_{\mathrm{prop}}^{-}} \int_{x_{\mathrm{prop}}^{-}}^{x_{\mathrm{prop}}^{+}} G(x) \, \mathrm{d}x \,, \tag{33}$$

to moment M_0. For high-stress nucleation, undrained thermal pressurization is the dominant weakening mechanism everywhere inside the rupture, and therefore $\langle G \rangle$ is independent of earthquake size. For low-strength nucleation, the relationship is more complex. A low M_0 limit exists due to the tradeoff of τ_0 and w, and such ruptures have ineffective thermal pressurization and therefore small $\langle G \rangle$. At larger τ_0, ruptures have significant thermal pressurization outside the rupture zone, so larger M_0 corresponds to larger $\langle G \rangle$ due to the increasing fraction of the rupture with effective thermal pressurization.

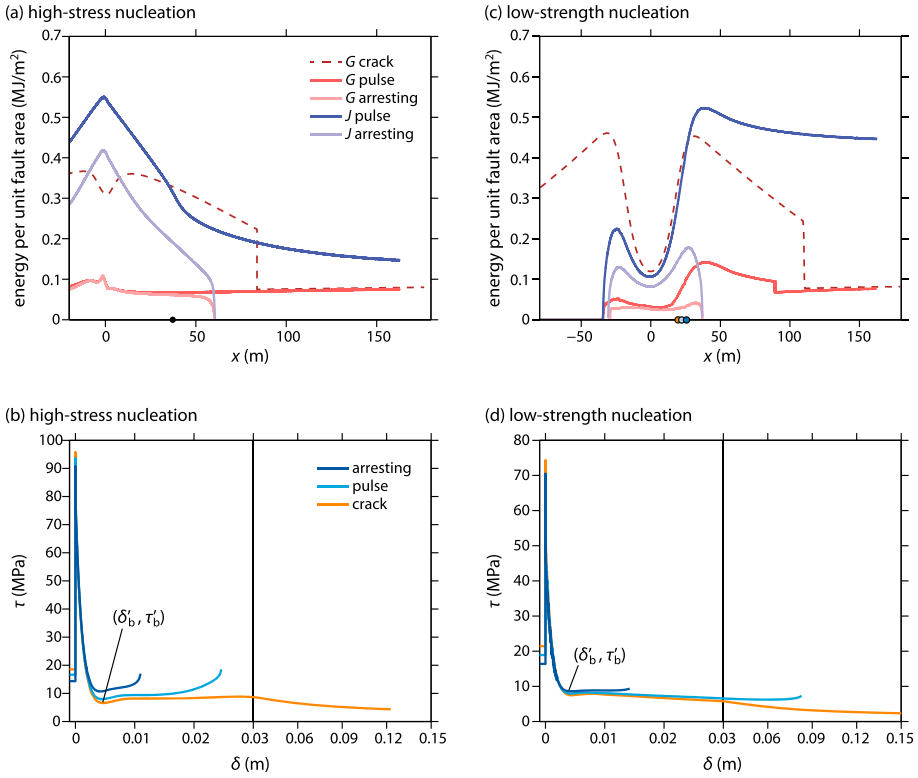

Figure 19. (a) Energy and work distributions on the fault for the high-stress simulations shown in Figures 7–9. $J(x)$ is the frictional sliding work, and $G(x)$ is the fracture energy as defined in equation (26). For sustained crack-like rupture, $G(x)$ is shown as calculated at the final simulation time step; its value is still growing at all x. (b) Sample $\tau(\delta)$ curves for the high-stress simulations at the position marked with the black dot in Figure 19a. Initial stress τ_0 is indicated by the value of τ to the left of $\delta = 0$ (δ is always positive). Initial stress minimum τ_b' and corresponding slip δ_b' are indicated for the crack-like rupture. The horizontal scale changes at $\delta = 0.03$ m. (c) J and G for the low-strength simulations shown in Figures 10 and 11. Line colors are the same as in Figure 19a]. (d) The $\tau(\delta)$ curves for the low-strength simulations at the positions corresponding to the same-colored dots in Figure 19c.

7.3.3. Comparison to Energy Budget of Natural Earthquakes

Since our simulations do not model other mechanisms of energy dissipation (such as off-fault fracturing or plastic yielding), energy not consumed in fault slip is radiated as seismic energy E_S. Thus, the computed values of E_S can be viewed as a theoretical upper bound on radiated energy for the earthquakes we simulate. Figure 20b displays the seismic radiation for each arresting rupture. Direct comparison to observed earthquakes is not possible because of the missing spatial dimension, but the ratio E_S/M_0 is expected to be similar between 2-D and 3-D since both numerator and denominator include integrals of slip over the rupture area. *Abercrombie* [1995, Figure 13] estimated E_S for several earthquakes near the Cajon Pass borehole with $0 < M_w < 3$, which led to values of E_S/M_0 from 10^{-7} to 10^{-4}, with higher values for larger M_0. The corresponding values of E_S for 2-D faulting are shown in Figure 20b and are generally lower than the E_S values obtained from our simulations.

Since our calculated values of E_S are higher than values inferred for real earthquakes, the seismic efficiencies E_S/E_W in Figure 20c are also higher than values inferred from seismic data. Because E_W is not observable with seismology, seismic efficiency is not typically reported for earthquakes. In laboratory earthquakes, however, complete τ-δ histories are recorded and seismic efficiencies can be calculated. *McGarr* [1994, 1999] reported values for a suite of such experiments as well as some deep mine earthquakes where E_W could be inferred and finds that $E_S/E_W \leq 0.06$ for all events. While that value is much smaller than those from our simulations, we note that large dynamic reductions in fault strength were not observed in the laboratory experiments. Strong dynamic weakening leads to large values of E_S/E_W if large slip occurs at low τ. In natural earthquakes, the discrepancy in seismic efficiency with our results may arise from either the absence of dynamic weakening or off-fault processes that reduce E_S.

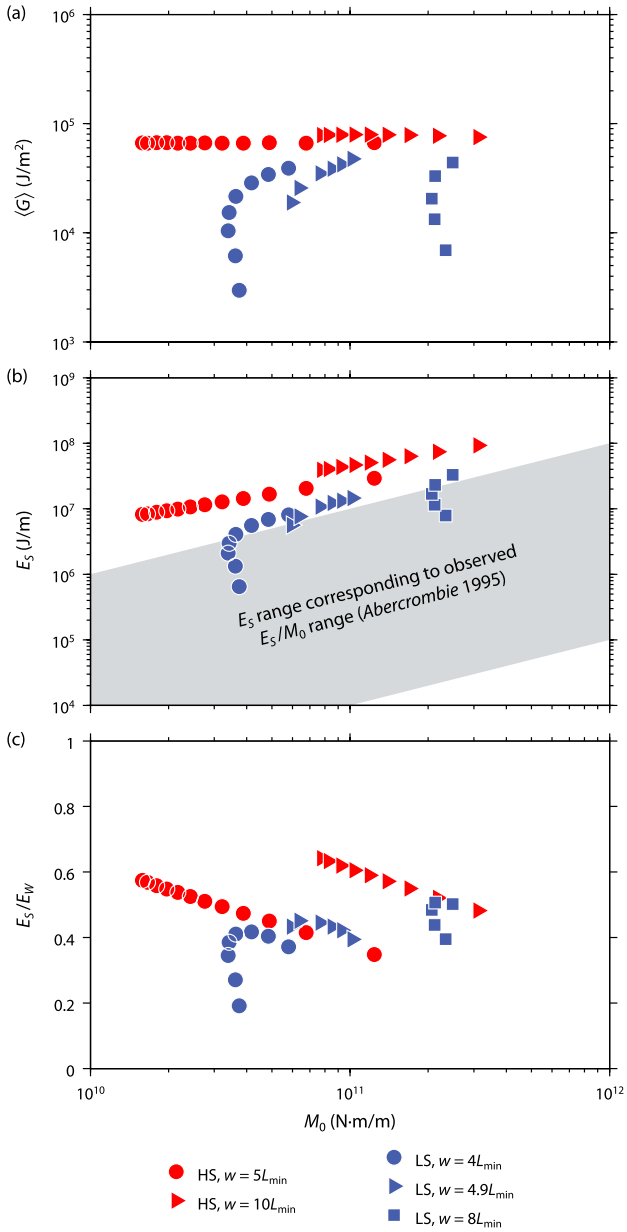

Figure 20. Energy quantities as a function of seismic moment. (a) Spatially averaged fracture energy. (b) Maximum radiated energy. The approximate range of observations by *Abercrombie* [1995] is shown. (c) Maximum seismic efficiency.

Another approach to provide seismological constraints on the earthquake energy budget is that of *Abercrombie and Rice* [2005], in which source parameters inferred from far-field seismograms are used to estimate the fracture energy of natural earthquakes. Using values of M_0 and R inferred from seismograms [*Brune*, 1970; *Madariaga*, 1976], stress drops can be inferred using *Eshelby* [1957] if the rupture is assumed to be a circular shear crack. Along with estimates of E_S [*Abercrombie*, 1995], mean fracture energy $\langle G \rangle$ may then be estimated, assuming that breakdown strength and final stress are equal and that the spatially averaged slip and fracture energy are representative of their local values. With the aforementioned assumptions, equation (32) can then be written as

$$\frac{E_S}{\pi R^2} = \left(\frac{\Delta\tau}{2} + \tau_b\right)\langle\delta\rangle - \tau_b\langle\delta\rangle - \langle G\rangle\,, \tag{34}$$

which rearranges to

$$\langle G\rangle = \left(\frac{\Delta\tau}{2} - \frac{\mu E_S}{M_0}\right)\frac{M_0}{\mu\pi R^2} = \left(\frac{\Delta\tau}{2} - \frac{\mu E_S}{M_0}\right)\langle\delta\rangle\,. \tag{35}$$

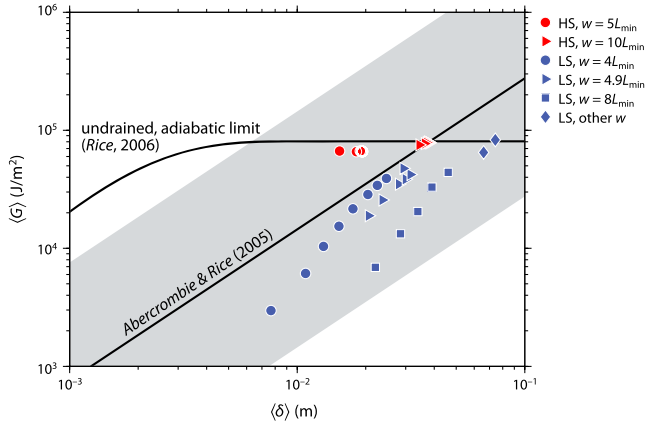

Figure 21. Values of mean slip $\langle \delta \rangle$ and mean fracture energy $\langle G \rangle$ from simulations with arresting ruptures. The empirical relationship of *Abercrombie and Rice* [2005] and its associated range of observations is shown by the line and shaded area. The undrained, adiabatic limit of G [*Rice*, 2006] is also shown.

Using equation (35), *Abercrombie and Rice* [2005] tabulated results of $\langle \delta \rangle$ and $\langle G \rangle$ from several dozen $M_w = 0$ to seven earthquakes and found that they follow the relationship

$$\frac{\langle G \rangle}{1\ \mathrm{MJ\ m^{-2}}} = 5.25 \left(\frac{\langle \delta \rangle}{1\ \mathrm{m}} \right)^{1.28}, \tag{36}$$

with all but two observations falling within a factor of 10 of that relationship. In Figure 21, we plot values of $\langle \delta \rangle$ and $\langle G \rangle$ from our simulations as well as the relationship of equation (36). We also show for reference *Rice's* [2006] expression for G for undrained, adiabatic thermal pressurization,

$$G(\delta) = \frac{\rho c_v \bar{\sigma} h \sqrt{2\pi}}{\Lambda} \left[1 - \left(1 + \frac{f \Lambda \delta}{\rho c_v h \sqrt{2\pi}} \right) \exp\left(- \frac{f \Lambda \delta}{\rho c_v h \sqrt{2\pi}} \right) \right], \tag{37}$$

which includes additional factors of $\sqrt{2\pi}$ to account for our Gaussian distribution of shear across the fault. All of our simulated arresting ruptures fall within the range of values obtained by *Abercrombie and Rice* [2005], with low-strength ruptures particularly closely following that trend. High-stress ruptures appear to follow a different trend in Figure 21, but that trend cannot extend for a wide range of $\langle \delta \rangle$. The smallest $\langle \delta \rangle$ shown for high-stress simulations represents the smallest earthquake possible given the material properties and effective stress conditions, while larger values of $\langle \delta \rangle$ require slip duration much longer those we observe in our arresting simulations (and well beyond the applicability of undrained, adiabatic thermal pressurization). Thus, all of our arresting rupture simulations remain consistent with the observations of *Abercrombie and Rice* [2005].

Given observational challenges regarding fracture energy, it is unlikely that nucleation style can be discerned in natural earthquakes, but our model predicts that extremely small earthquakes will have larger $\langle G \rangle$ for high-stress nucleation and smaller $\langle G \rangle$ for low-strength nucleation. The latter case may apply to a fraction of seismicity triggered by fluid injection. In that context, however, the triggering of aftershocks could be a high-stress process that complicates observational validation.

7.3.4. Fracture Energy in Sustained Ruptures

Our simple model is not capable of simulating large arresting ruptures due to both the simple stress distribution (uniform stress outside the nucleation region) and computational limits, but the mechanics may still be relevant to large ruptures that arrest in response to effects not present in our models. Such arrest processes may, for example, arise from stress or material variations far away from the nucleation zone that cannot sustain rupture. In such cases, slip may persist as in our crack-like simulations until wave-mediated arrest occurs, and fracture energy G grows with increasing slip δ (Figure 19).

Figure 22 shows the trajectory of G corresponding to the crack-like rupture of Figure 19b, calculated according to equation (26) at each time step. The initial large increase in G corresponds to the early slip when thermal pressurization is approximately undrained and adiabatic. The prediction of equation (37) closely matches the numerical result. After the initial strong weakening, restrengthening work H briefly becomes nonzero as

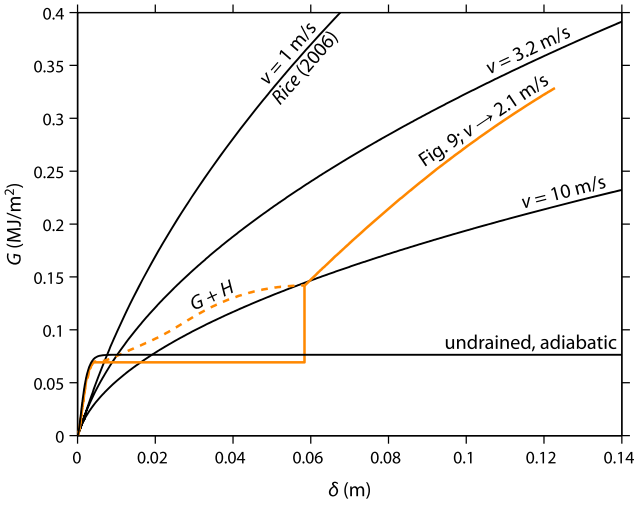

Figure 22. Fracture energy during sustained, crack-like slip. The value of G corresponding to the location of Figure 19b is shown in orange. Nonzero values of H as defined in Figure 18 are included in the dashed line. Predictions for G from the zero-width shear zone model of *Rice* [2006] are shown for various slip speeds.

defined in Figure 18 and is therefore included in Figure 22 (when further slip weakening overwhelms the restrengthening, H again vanishes). We may compare the value of G for larger δ to the *Rice's* [2006] analytical prediction for slip on a plane, with kinematically imposed slip at constant speed v and constant friction coefficient f. The slip-shear stress relationship is

$$\tau = f\bar{\sigma} \exp\left(\frac{\delta}{L^*}\right) \operatorname{erfc}\sqrt{\frac{\delta}{L^*}}\,, \tag{38}$$

with a characteristic slip distance

$$L^* = \frac{1}{v}\left[\frac{2\rho c_v\left(\sqrt{c_{\mathrm{hyd}}} + \sqrt{c_{\mathrm{th}}}\right)}{f\Lambda}\right]^2 . \tag{39}$$

It should be noted that the mathematical plane approximation is valid for distributed shear if slip occurs over a much longer timescale than diffusion across the shear zone and that the constant-velocity approximation is valid if the majority of slip occurs at $\sim v$. The latter condition is not yet satisfied in the simulation of Figure 22. Equation (38) is a monotonically decreasing function, so fracture energy is calculated to be [*Rice*, 2006]

$$\begin{aligned} G(\delta) &= \int_0^{\delta} \tau(\delta') - \tau(\delta)\, \mathrm{d}\delta' \\ &= f\bar{\sigma}L^*\left[\left(1 - \frac{\delta}{L^*}\right)\exp\left(\frac{\delta}{L^*}\right)\operatorname{erfc}\sqrt{\frac{\delta}{L^*}} - 1 + 2\sqrt{\frac{\delta}{\pi L^*}}\right] . \end{aligned} \tag{40}$$

Predictions given by equation (40) are shown in Figure 22 using various slip speeds and $f = 0.64$, which corresponds to the steady state value inside the rupture. While our simulation does not have constant slip speed, the bulk of the slip occurred as v steadied; the last 80% of the slip was at 2.1 to 2.9 m/s, so the comparison to constant-v predictions becomes more appropriate with larger δ. The value of $G(\delta)$ in our simulation appears to have a trajectory toward the prediction of *Rice* [2006]. For very large slip, equation (38) simplifies to

$$G(\delta) \approx \frac{f\bar{\sigma}\sqrt{\delta L^*}}{\sqrt{\pi}} \quad \text{for } \delta \gg L^*\,, \tag{41}$$

which has the interesting property of being independent of f since $L^* \propto f^{-2}$. Thus, we anticipate that values of G at large δ from our model will be consistent with those from other models that include thermal pressurization but use different friction laws. Further, *Rice* [2006] presents evidence that equation (38) is consistent with seismological observations.

Energy quantities obtained from our simulations compare favorably to values inferred or observed for natural earthquakes. Our small, arresting ruptures have stress drops ranging from 1 to 20 MPa and fracture energies of similar magnitude to those found by *Abercrombie and Rice* [2005]. In simulations of sustained rupture, which may correspond to larger ruptures brought to arrest by processes we do not model, fracture energies approach values shown by *Rice* [2006] to be consistent with seismologically inferred values. Frictional heating J in our simulations is also consistent with constraints of low-τ slip from surface heat flow observations [*Lachenbruch and Sass*, 1980] and rapid-response borehole studies following earthquakes [*Fulton et al.*, 2010, 2013].

7.4. Comparison to Steady-Pulse Solution

Garagash [2012] presents semianalytical solutions for steadily propagating dynamic and quasi-static slip pulses sustained by thermal pressurization on faults with a constant friction coefficient. The approach is different from ours, in that he postulates the existence of steady slip pulses and solves for pulse parameters that satisfy the governing equations of elasticity and diffusion. The constant friction model requires that slip is permissible only if $\tau = \tau_{\text{peak}}$ at the rupture tip and $\tau = f\sigma_{\text{eff}}$ behind it. With constant f, thermal pressurization provides a unique relationship between τ and v,

$$\tau(t) = f\bar{\sigma} - \frac{1}{\delta_c}\int_0^t \tau(t')v(t')\mathcal{K}(t-t';\gamma(y),c_{\text{th}},c_{\text{hyd}})\,\mathrm{d}t' \,, \tag{42}$$

where $\mathcal{K}$ is a convolution kernel that accounts for diffusion and the distribution of shear strain [*Garagash*, 2012, Appendix A]. At the pulse tip, where diffusion has yet to become significant (the undrained, adiabatic case), $\mathcal{K} \approx 1$. The characteristic slip-weakening distance δ_c (first defined in *Lachenbruch* [1980]) is

$$\delta_c = \frac{\rho c_v h\sqrt{2\pi}}{f\Lambda} \,, \tag{43}$$

which includes a factor of $\sqrt{2\pi}$ because of differing definitions of shear zone width h in *Garagash* [2012] and this work. The constitutive relationship (42) has some broad similarity to traditional rate- and state-dependent friction (8) in that shear stress depends on present slip rate and slip history, but it does result in different slip and stress trajectories than in our numerical models.

In *Garagash's* [2012] steady-pulse model, the fault is uniformly at shear stress τ_{bg} ahead of the stress concentration associated with the rupture, and the fault has a static frictional strength that corresponds to the magnitude of the shear stress at the pulse's leading tip τ_{peak}. Following the onset of slip, the shear stress drops to $\tau = f\sigma_{\text{eff}}$ and remains constant, such that restrengthening is entirely a consequence of diffusion. The rupture propagates at constant speed v_r as a pulse with width L, and the slip duration is thus $t_L = L/v_r$. Given the characteristic slip-weakening distance (43), a characteristic pulse length is thus

$$L_c = \frac{F(\frac{v_r}{c_s})\mu\delta_c}{\tau_{\text{peak}}} \,. \tag{44}$$

The length L_c can be understood as the minimum length of a region that is sufficiently compliant to relax stress τ_{peak} with slip δ_c. In equation (44), $F(\frac{v_r}{c_s})$ is a function that is monotonically decreasing with rupture velocity v_r, and for antiplane slip [*Kostrov and Nikitin*, 1970; *Rice*, 1980],

$$F(\tfrac{v_r}{c_s}) = \sqrt{1-\left(\frac{v_r}{c_s}\right)^2} \,. \tag{45}$$

Thus, fast ruptures ($F(\frac{v_r}{c_s}) \to 0$) have small characteristic pulse length. Finally, a characteristic pulse duration arises from the diffusion time across the shear zone

$$t^* = \frac{\pi h^2}{2\left(\sqrt{c_{\text{hyd}}}+\sqrt{c_{\text{th}}}\right)^2} \,. \tag{46}$$

With normalizations based on equations (43)–(46), *Garagash* [2012] numerically found solutions that satisfy the constitutive relationship (42) and the elasticity equation (6). His results for $c_{\text{th}} = c_{\text{hyd}}$ are displayed in

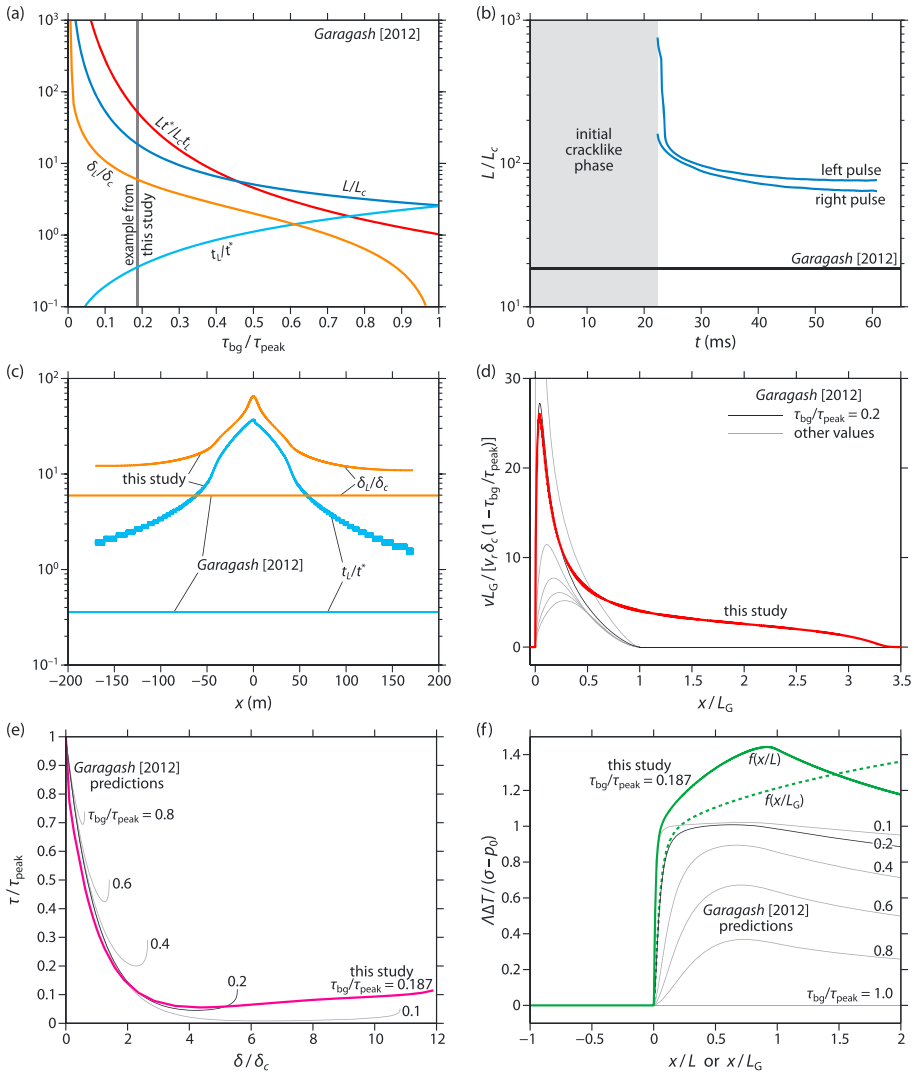

Figure 23. Predictions of steady-pulse characteristics from *Garagash* [2012] and comparison to our simulation shown in Figure 8 ($\tau_{bg}/\bar{\sigma} = 0.132$; $\tau_{bg}/\tau_{peak} = 0.187$). (a) Predictions of normalized values of pulse width L/L_c, pulse duration t_L/t^*, total slip δ_L/δ_c, and rupture velocity $Lt^*/t_L L_c$ for steadily propagating pulses on faults with scaled stress level τ_{bg}/τ_{peak}. The stress level for our simulation is marked with the vertical line. (b) Evolution of normalized pulse width during our simulation, compared to prediction (horizontal line). (c) Evolution of normalized total slip and pulse duration during our simulation, compared to predictions. (d) Normalized slip speed inside the pulse. The prediction for $\tau_{bg}/\tau_{peak} = 0.2$ is most applicable for comparing to our result. (e) Evolution of τ with δ. (f) Normalized temperature resulting from the slip pulse. For our result, the x dimension is scaled by both actual pulse width L and the predicted value L_G.

Figure 23a; normalized values of total slip δ_L/δ_c, pulse length L/L_c, pulse duration t_L/t^*, and rupture velocity $v_r t^*/L_c$ are shown as a function of τ_{bg}/τ_{peak}.

A summary of *Garagash's* [2012] results is shown in Figure 23a. For steady pulses to propagate at low τ_{bg} (and constant f) thermal pressurization is required to be very strong. At low stress this requires high slip velocity, which implies larger total slip δ_L and shorter pulse duration t_L. This results in rupture velocity near c_s such that L_c is small (equation (44)), implying longer-scaled pulse width L/L_c. For high τ_{bg}, *Garagash* [2012] predicts pulses with long t_L, small L, small δ_L, and slow rupture velocity.

The relationship between τ_{bg} and the intensity of thermal pressurization appears to be opposite what occurs in our simulations, with decaying pulses at low τ_{bg} and extremely energetic crack-like rupture at high τ_{bg}. The rupture mode itself is the significant difference; *Garagash* [2012] describes the characteristics of a self-sustaining pulse that satisfies the governing equations but does not address whether another rupture

type could also satisfy the governing equations. In our simulations, the governing equations are also satisfied by arresting ruptures at low τ_{bg} and crack-like ruptures at large τ_{bg}. Further, *Garagash* [2012] does not model how self-sustaining pulses are formed, and arresting or crack-like ruptures are clearly the most likely outcome of the nucleation process in our simulations. However, it remains a possibility that variations in the characteristics of the nucleating stress heterogeneity may allow for pulse-like rupture over a wide range of τ_{bg}, as in *Gabriel et al.* [2012].

Our simulations contain slip pulses sustained by thermal pressurization for a limited range of τ_{bg}, and we may compare the pulse-like behavior we observe in the high-stress simulation of Figures 6 and 8 to *Garagash's* [2012] model. In our simulations, $c_{hyd}/c_{th} = 4.269$, while the solutions in Figure 23a correspond to $c_{hyd} = c_{th}$. Within *Garagash's* [2012] analysis, our diffusivity contrast corresponds with negligible reductions of L/L_c and t_L/t^*, a few percent reduction of total slip δ_L/δ_c, and a few percent increase in ΔT, so the discrepancy does not preclude comparison. In our example simulation, $\tau_{bg} = 16.6$ MPa and $\tau_{peak} = 89$ MPa, so the prediction for $\tau_{bg}/\tau_{peak} = 0.2$ is most applicable. The friction coefficient f inside our pulse simulation remains roughly constant at $f = 0.64$ (Figure 6), which further facilitates comparison. Rupture velocities can be found from Figure 23a using

$$\frac{v_r}{c_s} = \left[1 + \left(\frac{\tau_{peak} c_s t^*}{\mu \delta_c} \frac{L_c t_L}{L t^*}\right)^2\right]^{-1}, \tag{47}$$

which is a rearranged form of equation (53) from *Garagash* [2012]. With $Lt^*/L_c t_L = 48$, equation (47) yields $v_r = 0.9907 c_s$, which is comparable to $v_r = 0.9904 c_s$ at the end of the simulation of Figure 8. Hence, the two models have nearly equivalent characteristic pulse length L_c.

Actual pulse length from our example simulation is longer than what *Garagash* [2012] predicts; the comparison is shown in Figure 23b. As the bilaterally propagating pulses emerge from the initial crack-like rupture, they initially have widths greater than $100L_c$. In Figure 8a, significant narrowing of the pulse is visible over the entire duration of the simulation, but Figure 23b shows that the pulses then stabilize at $L \approx 65L_c$, a value ~3.4 times larger than *Garagash's* [2012] prediction. The constant value of L/L_c after ~55 ms (particularly for the left pulse) suggests that the narrowing is a consequence of the pulse's acceleration rather than declining thermal pressurization leading to arrest. Total slip and pulse duration (Figure 23c) in our example simulation are also larger than *Garagash's* [2012] predictions, with the former converging on a value about double the prediction. Pulse duration t_L is still declining when the simulation is halted; that effect is presumably due to the ongoing increase in v_r and the corresponding decrease in L since $t_L = L/v_r$. We thus expect that it will converge to ~3.4 times the prediction.

The model of *Garagash* [2012] accurately predicts the behavior of our simulations near the pulse tip but diverges in the tail. Figure 23d shows our velocity in *Garagash's* [2012] normalization using the predicted pulse length L_G ($= L/3.4$) corresponding to that model. The two models are remarkably similar for $0 < x < 0.3L_G$, but farther back in the tail velocity remains elevated for a much longer distance. The evolution of τ with δ shown in Figure 23e shows similar correspondence for $\delta < 5\delta_c$; both breakdown slip δ_b and breakdown strength τ_b in our simulation are within 20% of the predicted values. However, the subsequent additional thermal pressurization in our model results in much more slip occurring during a prolonged restrengthening phase. Temperature, shown in Figure 23f, exhibits the largest discrepancy between the models. Our comparatively higher temperature for $0.1L_G < x < 0.3L_G$ is, however, consistent with *Garagash's* [2012] predictions for $c_{hyd} \gg c_{th}$, and the elevated temperature for $x > 0.3L_G$ is likely a consequence of the extended pulse tail with high v.

The differences in pulse tail behavior between our simulations and the constant friction pulse solutions of *Garagash* [2012] may arise from different elastic responses due to the existence of a nucleation zone, from different relationships between τ and v in the friction laws or from the coupling of the two effects. Extending the constant friction steady-pulse model to include rate- and state-dependent friction, *Viesca and Garagash* [2012] assert that rate/state effects can usually be neglected since $\delta_c \gg d_c$ and that variations in the friction coefficient for slip greater than a few d_c can be neglected. While friction varies little inside the pulse (Figure 6), shear heating depends on both traction and slip speed, which are coupled under rate/state friction. The prolonged slip in the pulse tail in our simulations indicates that rate/state effects likely should not be neglected in slip pulses with thermal pressurization.

7.5. Interaction With Other Fault Strength Mechanisms

Many additional physical processes likely occur during seismic slip. Dilatancy of fault zone material can offset the pore pressure rise resulting from thermal pressurization [*Segall and Bradley*, 2012], but the additional strengthening is partially offset by increased shear heating at higher stress [*Garagash and Rudnicki*, 2003]. Flash heating of asperity contacts [*Rice*, 2006; *Noda et al.*, 2009] substantially reduces the friction coefficient as slip exceeds a weakening velocity of ~0.1 m/s, which will reduce the effectiveness of thermal pressurization. Since flash heating is itself a strong dynamic weakening mechanism, it results in rupture propagation dynamics that are similar to those resulting from thermal pressurization. Yet the slip scale over which flash heating occurs is much smaller than that of thermal pressurization and results in a different earthquake energy balance. Plastic deformation of the near-fault material [*Dunham et al.*, 2011] limits the stress ahead of the rupture and reduces peak slip speeds, which may reduce thermal pressurization (and also flash heating). Further studies incorporating some or all of these mechanisms will be necessary to understanding how they interact with thermal pressurization, particularly during the transition from quasi-static slip to dynamic rupture. Comparison of such models to seismic and laboratory observations of small earthquakes may give insight into which processes are active at the onset of seismic slip.

8. Conclusion

We have modeled earthquake nucleation and initiation of seismic rupture on faults with heterogeneous stress, taking thermal pressurization into account at all phases. Thermal pressurization is capable of sustaining dynamic rupture when the background ratio of shear to normal stress is low, which is believed to occur during earthquakes in mature fault zones. For slip to nucleate, however, laboratory-derived frictional properties require a region with either high shear stress or low effective normal stress.

Stress heterogeneities that nucleate earthquakes must be sufficiently large that they can host a slip zone capable of accelerating to seismic speeds. That is, the stress conditions must allow formation of a region of width larger than $2L_{min}$ (equation (16)) in which friction reaches steady state. Since L_{min} is inversely proportional to effective normal stress, the minimum sizes of nucleation zones is larger for low-strength nucleation than it is for high-stress nucleation.

The process by which thermal pressurization and rate- and state-dependent friction together sustain rupture involves complex feedback. The stress concentration at the rupture tip results in elevated slip speed, resulting in a short period of extremely high frictional work rate τv. Substantial heating results in an increase in pore pressure, thereby decreasing effective normal stress. This produces a large strength drop behind the rupture tip, which sustains fast slip. Behind the rupture tip, slower slip speeds and lower shear stress result in lower frictional work, and the resulting thermal pressurization competes with diffusion to sustain slip.

Following high-stress nucleation, slip arrest occurs when thermal pressurization is insufficient to sustain rupture. If thermal pressurization behind the rupture tip is overwhelmed by diffusion, slip arrests and a slip pulse forms. These slip pulses are capable of propagating far into low-τ_{bg} regions. If, on the other hand, the increase in pore pressure balances or overwhelms diffusion, crack-like rupture occurs.

During and immediately following low-strength nucleation, thermal pressurization is weak. If it fails to become significant as the rupture grows, the rupture arrests. If thermal pressurization grows to a level that can sustain rupture, a crack-like rupture occurs. Slip pulses are possible if one side of the crack halts and emanates an arrest wave that chases the opposite rupture tip.

Background shear stress is the most important factor in controlling whether a rupture remains crack-like indefinitely, becomes a sustained pulse, or arrests. Larger values of τ_{bg} result in crack-like rupture, and lower values of τ_{bg} result in arresting ruptures. A narrow intermediate range of τ_{bg} results in sustained pulse-like rupture. Predicting a threshold value of τ_{bg} for crack-like rupture is difficult due to the dependence of τ on rupture history (via σ_{eff}), which is affected by the nucleation process.

Our simulated earthquakes occur at low average shear stress, and they consequently have small stress drops relative to the fault's static strength. These stress drops are on the order of 1–20 MPa, comparable to values inferred for small earthquakes. Arresting ruptures in our simulations have source dimension-moment relationships comparable to real earthquakes.

Fracture energy in our simulations exhibits varying scaling trends with earthquake magnitude or slip depending on rupture mode or nucleation style. In high-stress arresting ruptures, fracture energy is dominated by undrained thermal pressurization and is therefore independent of rupture size, whereas the reduced thermal pressurization following low-strength nucleation results in a proportionality between fracture energy and mean slip. In both cases of arresting ruptures, values of fracture energy computed from our simulations are comparable to those inferred for natural earthquakes [*Abercrombie*, 1995]. Simulations where ruptures are crack-like show increasing fracture energy as rupture proceeds. In this case, the initial undrained slip weakening with characteristic distance δ_c (equation (43)) is followed by continued weakening at low stress, which results in a growing value of fracture energy as slip increases.

The results of our simulations show that thermal pressurization and rate- and state-dependent friction are promising mechanisms to explain many aspects of faulting, such as the occurrence of earthquakes on faults with low stress and their apparent low-stress drops. To further validate these mechanisms, their behavior on faults with complex and physically plausible 3-D stress distributions must be studied. Such efforts, however, will be extremely computationally challenging due to the small spatial scales that must be resolved.

Appendix A: Numerical Methods

The long timescale of quasi-static nucleation and the extremely short timescale of fault evolution during dynamic slip pose different computational challenges. We use two codes that were developed independently to study those respective phases. In both codes, the fault is discretized in the x direction and the diffusive medium is discretized in the y direction. Both diffusion equations (1) and (3) are separately solved by finite differences only in the y direction (the much larger scale of the x direction makes diffusion in that dimension negligible). The elastic interaction $\psi(x,t)$ in equation (6) is calculated using the spectral boundary integral method with a periodic boundary condition on x.

For the nucleation phase, we use the quasi-dynamic code *FDRA* [*Bradley and Segall*, 2010; *Segall and Bradley*, 2012], which is capable of integrating the coupled diffusion system efficiently during times of slow evolution. In order to simulate diffusion over long timescales, *FDRA* uses a log-transformed discretization in y to accommodate both long-term diffusion over great lengths and short-term diffusion over small lengths near the fault. In order to avoid extremely short time steps required by small near-fault grid spacing, *FDRA* uses a semi-implicit time-stepping scheme in which fault slip and the elastic interaction are integrated using explicit time steps while diffusion substeps are computed implicitly. This semi-implicit method permits *FDRA* to solve the fully coupled friction-elasticity-diffusion system over multiple earthquake cycles (thousands of years) using a single workstation. Elasticity in *FDRA* is quasi-dynamic (that is, it includes the radiation damping term in (6) but approximates ψ with the quasi-static form), but calculations are halted before radiation becomes significant.

The dynamic rupture is simulated using *MDSBI* [*Dunham et al.*, 2003; *Noda et al.*, 2009], which includes full elastodynamics. The elastic interaction $\phi(x,t)$ becomes a convolution of the slip history with a known elastodynamic kernel [*Perrin et al.*, 1995; *Geubelle and Rice*, 1995]. Like *FDRA*, *MDSBI* uses explicit time steps for elasticity and friction with diffusion calculated during substeps. However, the diffusion substeps in *MDSBI* are calculated using explicit finite differences on a uniformly spaced grid.

Shortly before seismic radiation becomes significant, we export values of slip δ, fault state θ, shear stress τ, effective normal stress σ_{eff}, temperature T, and pore pressure p from *FDRA* to *MDSBI*. Quasi-static elasticity is appropriate when [*Rice et al.*, 2001]

$$q(v) = \frac{\mu v}{2\sqrt{a(b-a)}\sigma_{\text{eff}} c_s} \ll 1\,, \tag{A1}$$

which allows us to determine when to halt the quasi-static calculations. For the nominal values in Table 1, the criterion of equation (A1) evaluates to $v \ll 0.2$ m/s. In practice, we have found that there is no benefit to transitioning to the dynamic code when $q(v)$ is lower than 0.3. Thus, our quasi-static calculations are halted when $v(x,t) \approx 0.06$ m/s occurs somewhere on the fault (our evaluation of $q(v)$ accounts for the actual σ_{eff} due to thermal pressurization). We validated the accuracy of the transition between the two codes by conducting tests in which we exported simulations to *MDSBI* before dynamic effects become significant while allowing *FDRA* to continue to run. Provided that $q(v) < 0.3$, the two codes produce identical results for the duration of time before dynamic effects cause the simulations to diverge.

Since the two codes use different off-fault grid spacing, the temperature and pore pressure fields must be interpolated onto the grid to be used in *MDSBI*. We use $\Delta y \leq 0.16h$ (that is, the shear zone half width is more than 6.25 times the grid spacing), and the finite difference grid extends to $y_{max} \geq \sqrt{4c_{hyd}t_{dyn}}$, where t_{dyn} is the expected duration of the simulation. We tested longer off-fault grids and found them to be unnecessary in most cases. The *FDRA-MDSBI* transition thus discards much of the far-field p and T fields, but the values there do not evolve significantly during the short timescale of the dynamic calculations. The values of $p(x, y_{max})$ and $T(x, y_{max})$ remain fixed during the dynamic calculations. In many cases, we extended the x dimension relative to the *FDRA* mesh to accommodate long rupture propagation distances (we favor using the identical x discretization for both phases, but that can only be done with knowledge of how a dynamic simulation will unfold). In those cases, values of δ, θ, τ, ΔT, and Δp, which are all constant valued near the $\pm x$ edges of the *FDRA* mesh, are extended onto the newly created portion of the mesh.

Acknowledgments
We thank two anonymous reviewers for their constructive comments. One reviewer greatly assisted us in improving our comparison to the constant friction steady-pulse model. This research was supported by the National Science Foundation (EAR-0838267), the United States Geological Survey (G11AP20047), and the Southern California Earthquake Center (contribution 6005). SCEC is funded by NSF Cooperative Agreement EAR-1033462 and USGS Cooperative Agreement G12AC20038. No new data were used in producing this manuscript. All other data for this paper are properly cited and referred to in the reference list. Computer modeling code may be accessed via http://stuartschmitt.com/tp_weak_faults/.

References

Abercrombie, R. E. (1995), Earthquake source scaling relationships from −1 to 5 M_L using seismograms recorded at 2.5-km depth, *J. Geophys. Res.*, *100*(B12), 24,015–24,036.
Abercrombie, R. E., and J. R. Rice (2005), Can observations of earthquake scaling constrain slip weakening?, *Geophys. J. Int.*, *162*, 406–424, doi:10.1111/j.1365-246X.2005.02579.x.
Ague, J. J., J. Park, and D. M. Rye (1998), Regional metamorphic dehydration and seismic hazard, *Geophys. Res. Lett.*, *25*(22), 4221–4224.
Aki, K., and P. G. Richards (2002), *Quantitative Seismology*, 2nd ed., Univ. Sci. Books, Sausalito, Calif.
Ampuero, J.-P., and A. M. Rubin (2008), Earthquake nucleation on rate and state faults—Aging and slip laws, *J. Geophys. Res.*, *113*, B01302, doi:10.1029/2007JB005082.
Andrews, D. J. (2002), A fault constitutive relation accounting for thermal pressurization of pore fluid, *J. Geophys. Res.*, *107*(B12), 2363, doi:10.1029/2002JB001942.
Andrews, D. J., and Y. Ben-Zion (1997), Wrinkle-like slip pulse on a fault between different materials, *J. Geophys. Res.*, *102*(B1), 553–571.
Balfour, N. J., M. K. Savage, and J. Townend (2005), Stress and crustal anisotropy in Marlborough, New Zealand: Evidence for low fault strength and structure-controlled anisotropy, *Geophys. J. Int.*, *163*, 1073–1086, doi:10.1111/j.1365-246X.2005.02783.x.
Beroza, G., and T. Mikumo (1996), Short slip duration in dynamic rupture in the presence of heterogeneous fault properties, *J. Geophys. Res.*, *101*(B10), 22,449–22,460.
Bizzarri, A., and M. Cocco (2006a), A thermal pressurization model for the spontaneous dynamic rupture propagation on a three-dimensional fault: 1. Methodological approach, *J. Geophys. Res.*, *111*, B05303, doi:10.1029/2005JB003862.
Bizzarri, A., and M. Cocco (2006b), A thermal pressurization model for the spontaneous dynamic rupture propagation on a three-dimensional fault: 2. Traction evolution and dynamic parameters, *J. Geophys. Res.*, *111*, B05304, doi:10.1029/2005JB003864.
Bradley, A. M., and P. Segall (2010), Efficient numerical modeling of slow-slip and quasi-dynamic earthquke ruptures, *91*(52), Fall Meet. Suppl., Abstact S23A–2115.
Broberg, K. B. (1978), On transient sliding motion, *Geophys. J. R. Astron. Soc.*, *52*, 397–432.
Brune, J. N. (1970), Tectonic stress and the spectra of seismic shear waves from earthquakes, *J. Geophys. Res.*, *75*, 4997–5009.
Brune, J. N., T. L. Henyey, and R. F. Roy (1969), Heat flow, stress, and rate of slip along the San Andreas Fault, California, *J. Geophys. Res.*, *74*(15), 3821–3827.
Byerlee, J. (1978), Friction of rocks, *Pure Appl. Geophys.*, *116*, 615–626.
Chester, F. M., and J. S. Chester (2000), Stress and deformation along wavy frictional faults, *J. Geophys. Res.*, *105*(B10), 23,421–23,430.
Cochard, A., and R. Madariaga (1994), Dynamic faulting under rate-dependent friction, *Pure Appl. Geophys.*, *142*(3/4), 419–445.
Day, S. M. (1982), Three-dimensional finite difference simulation of fault dynamics: Rectangular faults with fixed rupture velocity, *Bull. Seismol. Soc. Am.*, *72*, 705–727.
Dieterich, J. H. (1979), Modeling of rock friction: 1. Experimental results and constitutive equations, *J. Geophys. Res.*, *84*(B5), 2161–2168.
Dieterich, J. H. (1992), Earthquake nucleation on faults with rate- and state-dependent strength, *Tectonophysics*, *211*, 115–134.
Dieterich, J. H. (1994), A constitutive law for rate of earthquake production and its application to earthquake clustering, *J. Geophys. Res.*, *99*(B2), 2601–2619.
Dunham, E. M., P. Favreau, and J. M. Carlson (2003), A supershear transition mechanism for cracks, *Science*, *299*, 1557–1559.
Dunham, E. M., D. Belanger, L. Cong, and J. E. Kozdon (2011), Earthquake ruptures with strongly rate-weakening friction and off-fault plasticity, part 1: Planar faults, *Bull. Seismol. Soc. Am.*, *101*(5), 2296–2307, doi:10.1785/0120100075.
Eshelby, J. D. (1957), The determination of the elastic field of an ellipsoidal inclusion and related problems, *Proc. R. Soc. London*, *241*, 376–396.
Freund, L. B. (1979), The mechanics of dynamic shear crack propagation, *J. Geophys. Res.*, *84*, 2199–2209.
Fulton, P. M., R. N. Harris, D. M. Saffer, and E. E. Brodsky (2010), Does hydrologic circulation mask frictional heat on faults after large earthquakes?, *J. Geophys. Res.*, *115*, B09402, doi:10.1029/2009JB007103.
Fulton, P. M., E. E. Brodsky, Y. Kano, J. Mori, F. Chester, T. Ishikawa, R. N. Harris, W. Lin, N. Eguchi, S. Toczko, Expedition 343, 343T, and KR13-08 Scientists (2013), Low coseismic friction on the Tohoku-Oki fault determined from temperature measurements, *Science*, *342*(6163), 1214–1217, doi:10.1126/science.1243641.
Gabriel, A.-A., J.-P. Ampuero, L. A. Dalguer, and P. M. Mai (2012), The transition of dynamic rupture styles in elastic media under velocity-weakening friction, *J. Geophys. Res.*, *117*, B09311, doi:10.1029/2012JB009468.
Garagash, D. I. (2012), Seismic and aseismic slip pulses driven by thermal pressurizaion of pore fluid, *J. Geophys. Res.*, *117*, B04314, doi:10.1029/2011JB008889.
Garagash, D. I., and L. N. Germanovich (2012), Nucleation and arrest of dynamic slip on a pressurized fault, *J. Geophys. Res.*, *117*, B10310, doi:10.1029/2012JB009209.
Garagash, D. I., and J. W. Rudnicki (2003), Shear heating of a fluid-saturated slip-weakening dilatant fault zone: 1. Limiting regimes, *J. Geophys. Res.*, *108*(B2), 2121, doi:10.1029/2001JB001653.
Geubelle, P. H., and J. R. Rice (1995), A spectral method for three-dimensional elastodynamic fracture problems, *J. Mech. Phys. Solids*, *43*, 1791–1824.

Habib, P. (1967), Sur un mode de glissement des massifs rocheaux, *C. R. Hebd. Séanc. Acad. Sci.*, *264*, 151–153.
Heaton, T. H. (1990), Evidence for and implications of self-healing pulses of slip in earthquake rupture, *Phys. Earth Planet. Inter.*, *60*, 1–20.
Heidbach, O., M. Tingay, A. Barth, J. Reinecker, D. Kurfeß, and B. Müller (2008), The World Stress Map database release 2008, equatorial scale 1:46,000,000, Commission for the Geological Map of the World, Paris, doi:10.1594/GFZ.WSM.Rel2008.
Huang, Y., and J.-P. Ampuero (2011), Pulse-like ruptures induced by low-velocity fault zones, *J. Geophys. Res.*, *116*, B12307, doi:10.1029/2011JB008684.
Johnson, E. (1990), On the initiation of unidirectional slip, *Geophys. J. Int.*, *101*, 124–132.
Kano, Y., J. Mori, R. Fujio, H. Ito, T. Yanagidani, S. Nakao, and K.-F. Ma (2006), Heat signature on the Chelungpu fault associated with the 1999 Chi-Chi, Taiwan earthquake, *Geophys. Res. Lett.*, *33*, L14306, doi:10.1029/2006GL026733.
Kostrov, B. V., and L. V. Nikitin (1970), Some general problems of mechanics of brittle fracture, *Arch. Mech. Stos.*, *22*, 749–775.
Lachenbruch, A. (1980), Frictional heating, fluid pressure, and the resistance to fault motion, *J. Geophys. Res.*, *85*(B11), 6097–6112.
Lachenbruch, A., and J. H. Sass (1980), Heat flow and energetics of the San Andreas fault zone, *J. Geophys. Res.*, *85*(B11), 6185–6223.
Lapusta, N., J. R. Rice, Y. Ben-Zion, and G. Zheng (2000), Elastodynamic analysis for slow tectonic loading with spontaneous rupture episodes on faults with rate- and state-dependent friction, *J. Geophys. Res.*, *105*(B10), 23,765–23,790.
Lee, T. C., and P. T. Delaney (1987), Frictional heating and pore pressure rise due to fault slip, *Geophys. J. R. Astron. Soc.*, *88*(3), 569–591.
Liu, Y., and J. R. Rice (2005), Aseismic slip transients emerge spontaneously in three-dimensional rate and state modeling of subduction earthquake sequences, *J. Geophys. Res.*, *110*, B08307, doi:10.1029/2004JB003424.
Lockner, D. H., H. Naka, H. Tanaka, H. Ito, and R. Ikeda (2000), Permeability samples and strength of core samples from the Nojima fault of the 1995 Kobe earthquake, in *Proceedings of the International Workshop on the Nojima Fault Core and Borehole Data Analysis, Tsukuba, Japan, Nov 22–23 (1999)*, edited by H. Ito et al., *U.S. Geol. Surv. Open File Rep. 00-129*, pp. 147–152, Matsuyama, Jpn.
Madariaga, R. (1976), Dynamics of an expanding circular fault, *Bull. Seismol. Soc. Am.*, *66*, 639–666.
Marone, C. (1998), Laboratory-derived friction laws and their application to seismic faulting, *Annu. Rev. Earth Planet. Sci.*, *26*, 643–696.
Mase, C. W., and L. Smith (1985), Pore fluid pressures and frictional heating on a fault surface, *Pure Appl. Geophys.*, *122*, 583–607.
Mase, C. W., and L. Smith (1987), Effects of frictional heating on the thermal, hydrologic, and mechanical response of a fault, *J. Geophys. Res.*, *92*(B7), 6249–6272.
McGarr, A. (1994), Some comparisons between mining-induced and laboratory earthquakes, *Pure Appl. Geophys.*, *142*, 467–489.
McGarr, A. (1999), On relating apparent stress to the stress causing earthquake fault slip, *J. Geophys. Res.*, *104*(B2), 3003–3011.
Melosh, H. J. (1979), Acoustic fluidization: A new geologic process?, *J. Geophys. Res.*, *84*(B13), 7513–7520.
Nakatani, M. (2001), Conceptual and physical clarification of rate and state friction: Frictional sliding as a thermally activated rheology, *J. Geophys. Res.*, *106*(B7), 13,347–13,380.
Noda, H., and N. Lapusta (2010), Three-dimensional earthquake sequence simulations with evolving temperature and pore pressure due to shear heating: Effect of heterogeneous hydraulic diffusivity, *J. Geophys. Res.*, *115*, B12314, doi:10.1029/2010JB007780.
Noda, H., E. M. Dunham, and J. R. Rice (2009), Earthquake ruptures with thermal weakening and the operation of major faults at low overall stress levels, *J. Geophys. Res.*, *114*, B07302, doi:10.1029/2008JB006143.
Okubo, P. G. (1989), Dynamic rupture modeling with laboratory-derived constitutive relations, *J. Geophys. Res.*, *94*(B9), 12,321–12,335.
Perrin, G., J. R. Rice, and G. Zheng (1995), Self-healing slip pulse on a frictional interface, *J. Mech. Phys. Solids*, *43*, 1461–1495.
Ratchkovski, N. A. (2003), Change in stress directions along the central Denali fault, Alaska after the 2002 earthquake sequence, *Geophys. Res. Lett.*, *30*(19), 2017, doi:10.1029/2003GL017905.
Rice, J. R. (1980), The mechanics of earthquake rupture, in *Physics of the Earth's Interior, Proceedings of International School Physics "Enrico Fermi"*, vol. 78, edited by A. M. Dziewonski and E. Boschi, pp. 555–649, Italian Phys. Soc. Bologna, and North Holland Publ. Co., Amsterdam.
Rice, J. R. (1993), Spatio-temporal complexity of slip on a fault, *J. Geophys. Res.*, *98*(B6), 9885–9907, doi:10.1029/93JB00191.
Rice, J. R. (2006), Heating and weakening of faults during earthquake slip, *J. Geophys. Res.*, *111*, B05311, doi:10.1029/2005JB004006.
Rice, J. R., N. Lapusta, and K. Ranjith (2001), Rate and state dependent friction and the stability of sliding between elastically deformable solids, *J. Mech. Phys. Solids*, *49*, 1865–1898.
Rivera, L., and H. Kanamori (2005), Representations of the radiated energy in earthquakes, *Geophys. J. Int.*, *162*(1), 148–155, doi:10.1111/j.1365-246X.2005.02648.x.
Rubin, A. M., and J.-P. Ampuero (2005), Earthquake nucleation on (aging) rate and state faults, *J. Geophys. Res.*, *110*, B11312, doi:10.1029/2005JB003686.
Ruina, A. (1983), Slip instability and state variable friction laws, *J. Geophys. Res.*, *88*(B12), 10,359–10,370.
Schmitt, S. V., P. Segall, and T. Matsuzawa (2011), Shear heating-induced thermal pressurization during earthquake nucleation, *J. Geophys. Res.*, *116*, B06308, doi:10.1029/2010JB008035.
Segall, P. (2010), *Earthquake and Volcano Deformation*, Princeton Univ. Press, Princeton and Oxford.
Segall, P., and A. Bradley (2012), The role of thermal pressurization and dilatancy in controlling the rate of fault slip, *J. Appl. Mech.*, *79*(3), 31013, doi:10.1115/1.4005896.
Segall, P., and J. R. Rice (1995), Dilatancy, compaction, and slip instability of a fluid-infiltrated fault, *J. Geophys. Res.*, *100*(B11), 22,155–22,171.
Segall, P., and J. R. Rice (2006), Does shear heating of pore fluid contribute to earthquake nucleation?, *J. Geophys. Res.*, *111*, B09316, doi:10.1029/2005JB004129.
Sibson, R. H. (1973), Interactions between temperature and pore-fluid pressure during earthquake faulting and a mechanism for partial or total stress relief, *Nat. Phys. Sci.*, *243*(126), 66–68.
Suzuki, T., and T. Yamashita (2006), Nonlinear thermoporoelastic effects on dynamic earthquake rupture, *J. Geophys. Res.*, *111*, B03307, doi:10.1029/2005JB003810.
Tinti, E., P. Spudich, and M. Cocco (2005), Earthquake fracture energy inferred from kinematic rupture models on extended faults, *J. Geophys. Res.*, *110*, B12303, doi:10.1029/2005JB003644.
Townend, J., and M. D. Zoback (2004), Regional tectonic stress near the San Andreas fault in central and southern California, *Geophys. Res. Lett.*, *31*, L15S11, doi:10.1029/2003GL018918.
Viesca, R. C., and D. Garagash (2012), Steady slip pulses on faults with rate- and state-dependent friction and multiple thermal weakening mechanisms, Abstract S21B-2435 presented at 2012 Fall Meeting, AGU, San Francisco, Calif., 3–7 Dec.
Viesca, R. C., and J. R. Rice (2012), Nucleation of slip-weakening rupture instability in landslides by localized increase of pore pressure, *J. Geophys. Res.*, *117*, B03104, doi:10.1029/2011JB008866.
Vredevoogd, M. A., D. D. Oglesby, and S. K. Park (2007), Fluid pressurization due to frictional heating on a fault at a permeability contrast, *Geophys. Res. Lett.*, *34*, L18304, doi:10.1029/2007GL030754.

Wibberley, C. A. J., and T. Shimamoto (2003), Internal structure and permeability of major strike-slip fault zones: The Median Tectonic Line in Mie Prefecture, Southwest Japan, *J. Struct. Geol.*, *25*, 59–78.

Zheng, G., and J. R. Rice (1998), Conditions under which velocity-weakening friction allows for a self-healing versus a cracklike mode of rupture, *Bull. Seismol. Soc. Am.*, *88*(6), 1466–1483.

Zoback, M. D., et al. (1987), New evidence for the state of stress on the San Andreas fault system, *Science*, *238*, 1105–1111.